

AD A095063

10  
12  
14  
USAFA-TN-81-1

DEPARTMENT OF AERONAUTICS  
DEAN OF THE FACULTY  
UNITED STATES AIR FORCE ACADEMY  
COLORADO 80840

LEVEL II

6  
MEASUREMENT OF CANARD  
WAKES

⑨Fiscal-Sept. 1  
1 Oct 79 - 30 Sep 80

TECHNICAL NOTE

USAFA-TN-81-1

DTIC  
ELECTE  
FEB 17 1981  
S D  
-E-

10  
G. SISSON  
R. CRANDALL

11  
2 FEB [REDACTED] 81

12  
151

APPROVED FOR PUBLIC RELEASE: DISTRIBUTION UNLIMITED

011550

7/3

81 2 13 028

BBG FILE COPY

This document consists of two monographs worthy of publication. The United States Air Force Academy vouches for the quality of research, without necessarily endorsing the opinions and conclusions of the authors.

The Technical Note has been cleared for open publication and/or public release by the appropriate Office of Information in accordance with AFR 190-17 and DODD 5230.9. There is no objection to unlimited distribution of this Technical Note to the public at large, or by DDC to the National Technical Information Service.

This Technical Note has been reviewed and is approved for publication.

*M.D. Bacon*  
M.D. BACON, Colonel, USAF  
Director of Research and  
Continuing Education

AC 96 678

FORWARD

This technical note is the final report covering the period 1 Oct 79 to 30 Sep 80 in response to project order number NASA PRN A-65764B sponsored by NASA Ames Research Center and administered by Mr Tom Gregory. Lt Col R. W. Gallington and Capt G. Sisson were principal investigators and were aided by staff and cadets at the Air Force Academy. This technical note consists of two separate papers. The first covers the manufacture and calibration of miniature seven hole probes and is a reprint of an article in the Aeronautics Digest Spring/Summer 1980 edition, USAFA-TR-80-17. The second paper covers the flow field data collection and presentation, and will be published in the Aeronautics Digest Spring/Summer 1981 edition. Together, the two papers describe the entire process developed to quickly and economically measure the flow field properties in canard model wakes.

STW 12-4

Accession For	
NTIS GRA&I	<input checked="" type="checkbox"/>
DTIC TAB	<input type="checkbox"/>
Unannounced	<input type="checkbox"/>
Justification	
By _____	
Distribution/ _____	
Availability Codes	
Dist	Avail and/or Special
A	

MEASUREMENT OF VERY LARGE FLOW ANGLES  
WITH NON-NULING SEVEN-HOLE PROBES

R.W. Gallington\*

**Abstract**

This paper describes a method for measuring local direction and total and static pressures of a flow by means of a fixed probe, provided that the local air flow does not make an angle of more than 80 degrees with the axis of the probe. Rapid surveys of the wakes formed behind variously-configured lifting body models during wind tunnel testing require such a probe. The probe is easily manufactured from standard-sized tubing materials. The power series calibration method used with the probe results in explicit polynomial expressions for the desired aerodynamic properties. The calibration method is easily programmed on a data acquisition system. This paper includes an example of a complete incompressible calibration and discusses a logical method for extending the calibration technique to compressible flows.

**I. Introduction**

When testing aerodynamic shapes in the wind tunnel, researchers are often interested in obtaining information about the flow field created by these shapes. To this end, numerous techniques have been devised to make the flow patterns visible. These techniques are helpful in visualizing the flow, but actual quantitative information about the size and direction of the velocity field ultimately depend on a direct flow measurement. One of the oldest known quantitative techniques involves the use of a pressure probe. The earliest of these probes was developed by Henri Pitot in the 1700's. Over the years Pitot tubes have been made extremely small so as not to disturb the flow field with the intruding probe. Additionally, the old ideas of measuring stagnation pressure directly, requiring near perfect alignment of the probe with the flow direction (that is, extremely small flow angles), have given way to small probes with multiple ports and a relaxation of the near-zero flow angle requirement.

In a previous paper we discussed the calibration of one such small multiple-hole probe, the five-hole probe (Ref. 1). As we reported in Ref. 1, and as Wuest reported earlier (Ref. 2), the probes could not be calibrated to give useful flow information beyond flow angles of 30 degrees measured from the flow direction to the probe axis, a limitation shared with triaxial, hot wire probes (Ref. 3). Unfortunately, many interesting flows such as wing wakes involve flow fields containing concentrated vortices. In these wakes larger flow angles occur (Ref. 4) which until now could only be measured by means of elaborate mechanical devices such as nulling probes or the laser doppler velocimeter. These too have limitations; the laser doppler velocimeter, for example, has geometrical limitations when the required optical paths are considered (Ref. 5).

Practical methods for calibrating pressure probes are rapidly improving as experience with automated data acquisition systems increases. Some very general methods of calibra-

---

\*Lt Col, USAF, Tenure Associate Professor of Aeronautics, DFAN

tion described only conceptually a few years ago (Ref. 6) can now be conveniently applied because of the use of automated data systems. These calibration methods effectively remove the requirement for the probe to directly measure certain fluid pressures (such as total and static pressures) or to generate simple coefficients which vary almost in a linear relation to changes in the probe's angle of attack or angle of sideslip measured from the flow direction to the probe axis. The requirement to compensate for these nonlinear effects is factored into the calibration procedure. Thus, the design of the probe and the technique of manufacturing them becomes primarily governed by considerations such as ease of manufacture and the need to provide adequate flow areas in the probe holes to enhance pneumatic response of sensors connected by tubing to the probe holes.

This paper describes a unique probe design, manufacturing process, and calibration procedure which in combination permit the accurate measurement of the total pressure of the flow, the static pressure of the flow, and all three components of fluid flow velocity all at the probe location and through total flow angles of 80 degrees measured from the flow direction to the probe axis. Further, this method is relatively fast in measuring these characteristics.

In order to approach this subject in an orderly manner, the paper first describes the reason for building a seven-hole probe by examining the pressure coefficients for a five-hole probe and comparing them to those for a seven-hole probe. Then, the desired form of these calibration equations which makes use of these variable pressure coefficients is described. The method we use for computing the numerous constant calibration coefficients of the power series in the variable pressure coefficients is also described. Next we describe the manufacturing procedure for a seven-hole probe and other necessary apparatus and the procedures necessary to calibrate a probe. The final section of the paper describes the results when the probe and computation method are applied to a probe calibrated for measuring incompressible fluid flows.

## II. Rationale for a Seven-Hole Probe

To describe why the seven-hole probe is a desirable design choice for measuring flow when the probe is positioned at high angles of attack and sideslip, one must first understand why the more commonly used five-hole probe fails at high flow angles.

### A. Five-Hole Probes at High Flow Angles

Refer to Figure 1. One can see that at high angles of attack one of the side ports in the five-hole probe becomes almost a stagnation port while the opposite port measures the pressure in the separated wake. Neither of these pressures is sensitive to small changes in angle of attack. Specifically (still referring to Figure 1), the commonly used pressure coefficient,  $C_a$ , which will yield the angle of attack the probe makes to the flow when the pressure coefficient is inserted into the appropriate calibra-

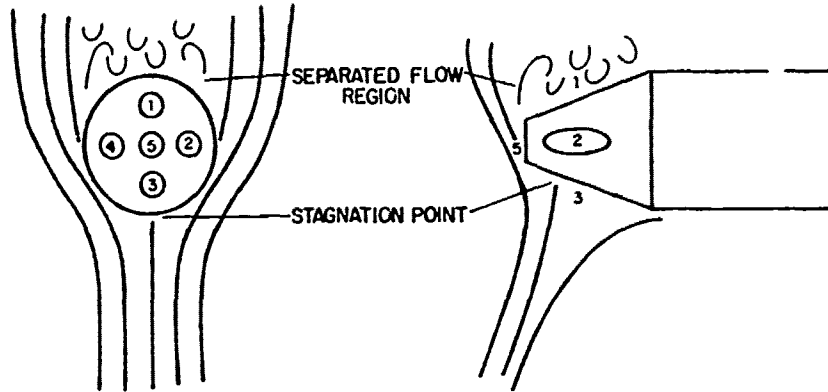


Figure 1. Flow Pattern Over Five-Hole Probe  
at High Angle of Attack

tion equation, is given by Eqn. (1):

$$C_{\alpha} = \frac{P_3 - P_1}{P_5 - \frac{P_1 + P_2 + P_3 + P_4}{4}} \quad (1)$$

This pressure coefficient, however, becomes independent of the angle of attack at high flow angles. Similarly,  $C_{\beta}$ , the coefficient intended to yield sideslip information, becomes independent of the angle it is intended to measure at large angles of sideslip.

In fact, at high flow angles it is the center port pressure which is the most dependent on flow angle in contrast to low flow angle situations where the center port pressure is nearly independent of flow angle (that is, in the usual case the center port measures stagnation pressure). Therefore, a coefficient which is sensitive to flow angle at high flow angles might be  $C_{\theta_3}$  which includes the pressure difference between the new stagnation port and the center port. This is mathematically expressed by this equation:

$$C_{\theta_3} = \frac{P_3 - P_5}{P_3 - \frac{P_4 + P_2}{2}}, \quad (2)$$

As long as the fluid velocity is generally upward across the probe, this coefficient could give us flow angle information. (Other coefficients could be defined for other quadrants.) To determine the azimuthal angle of the velocity vector, one might consider the pressure coefficient  $C_{\phi_3}$  given by the following equation:

$$C_{\phi_3} = \frac{P_2 - P_4}{P_3 - \frac{P_2 - P_4}{2}} \quad (3)$$

However, this pressure coefficient will be insensitive to the azimuthal position of the probe if the flow in the cross flow plane is attached beyond ports 2 and 4 as in ideal air flow around a cylinder. Certainly the flow will not be reliably attached

or separated over these ports for the whole range of desired measurement angles, thereby introducing uncertainties into any measurement that might be made at a particular instant or point. In general, past experience has shown that it is preferable to use only pressure ports under attached flows. Thus, separated air flow reduces the number of ports which can be applied to a given measurement situation and since at least one of the four peripheral ports will always be in separated flow, the five-hole probe is a bad choice for measuring high flow angles.

#### B. Seven-Hole Probe at High Angles

With the seven-hole probe illustrated in Figure 2, the problem of finding a



Figure 2. Flow Pattern Over Seven-Hole Probe  
at High Angle of Attack

roll-angle-sensitive pressure coefficient is solved by using the pressure coefficients obtained directly from measured pressures inserted into the following equations:

$$C_{\theta_4} = \frac{P_4 - P_7}{P_4 - \frac{P_3 + P_5}{2}}, \quad C_{\phi_4} = \frac{P_3 - P_5}{P_4 - \frac{P_3 + P_5}{2}} \quad (4)$$

which apply for the case when the velocity vector is in a pie-shaped sector containing the 60-degree region directly beneath the probe. Note here that we are assured that the pressure ports we are interested in will always be in an attached flow region.

To determine the flow angles in sectors where the oncoming velocity is other than directly below the probe, additional coefficients are needed. The required set of pressure coefficients are as follows:

$$C_{\theta_1} = \frac{P_1 - P_7}{P_1 - \frac{P_2 + P_6}{2}}, \quad C_{\phi_1} = \frac{P_6 - P_2}{P_1 - \frac{P_2 + P_6}{2}}$$

$$\begin{aligned}
 C_{\theta_2} &= \frac{P_2 - P_7}{P_2 - \frac{P_1 + P_3}{2}}, & C_{\phi_2} &= \frac{P_1 - P_3}{P_2 - \frac{P_1 + P_3}{2}} \\
 C_{\theta_3} &= \frac{P_3 - P_7}{P_3 - \frac{P_2 + P_4}{2}}, & C_{\phi_3} &= \frac{P_2 - P_4}{P_3 - \frac{P_2 + P_4}{2}} \\
 C_{\theta_4} &= \frac{P_4 - P_7}{P_4 - \frac{P_3 + P_5}{2}}, & C_{\phi_4} &= \frac{P_3 - P_5}{P_4 - \frac{P_3 + P_5}{2}} \\
 C_{\theta_5} &= \frac{P_5 - P_7}{P_5 - \frac{P_4 + P_6}{2}}, & C_{\phi_5} &= \frac{P_4 - P_6}{P_5 - \frac{P_4 + P_6}{2}} \\
 C_{\theta_6} &= \frac{P_6 - P_7}{P_6 - \frac{P_5 + P_1}{2}}, & C_{\phi_6} &= \frac{P_6 - P_7}{P_6 - \frac{P_5 + P_1}{2}}
 \end{aligned} \tag{5}$$

where each of the subscripts, 1 through 6, refers to a specific 60-degree sector in the total 360-degree area around the probe. By using these pressure coefficients the limit to the angular range available for accurate measurement of fluid properties will occur only when  $P_n$  ( $n$  refers to 1 through 6, depending on the sector) begins to decrease as rapidly as  $P_7$  as the angle between the velocity vector and the probe axis,  $\theta$ , increases indicating separated flow. This, however, does not occur on the seven-hole probe until  $\theta$  increases beyond 80 degrees.

#### C. Seven-Hole Probe at Low Angles

When the velocity makes a low angle with respect to the probe axis two pressure coefficients can be described which make use of all seven measured pressures. To this end we first define three pressure coefficients as follows:

$$C_{\alpha_1} = \frac{P_4 - P_1}{P_7 - \bar{P}_{1-6}}, \quad C_{\alpha_2} = \frac{P_3 - P_6}{P_7 - \bar{P}_{1-6}}, \quad C_{\alpha_3} = \frac{P_2 - P_5}{P_7 - \bar{P}_{1-6}} \tag{6}$$

To understand what these pressure coefficients mean, consider the coordinate system shown in Figure 3. Here two coordinate systems, one involving  $C_{\alpha_1}$ ,  $C_{\alpha_2}$ , and  $C_{\alpha_3}$ , and the other involving  $C_\alpha$  and  $C_\beta$  are overlaid.  $C_\alpha$  and  $C_\beta$  are the pressure coefficients that would have been measured if a five-hole probe had been used.

We see that the position of the tail of the oncoming velocity vector can be described in only one way in the  $C_\alpha$ ,  $C_\beta$  system using an equation like Eqn. (1) to yield

$$C_\alpha = 3, \quad C_\beta = 0.5 \tag{7}$$

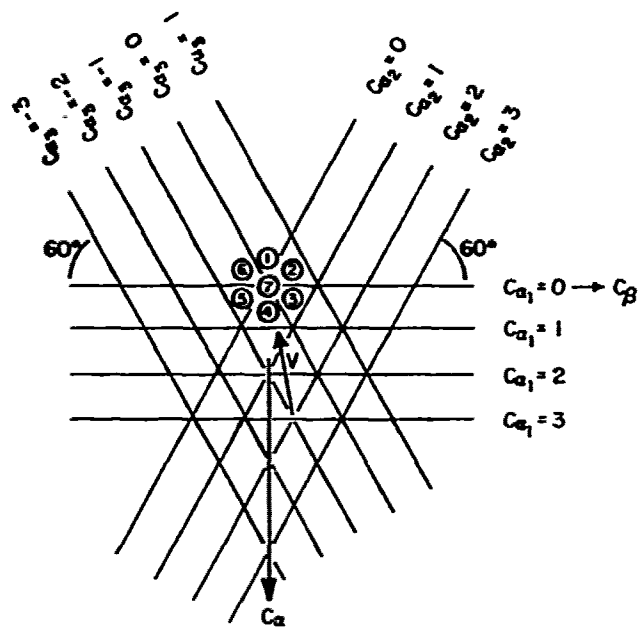


Figure 3. Coordinate System Suitable for the Calibration of Seven-Hole Probes at Low Angles

But in the  $C_{\alpha_1}$ ,  $C_{\alpha_2}$ ,  $C_{\alpha_3}$  system, the description can take any one of three forms, namely:

$$\begin{aligned}
 C_{\alpha_1} &= 3, & C_{\alpha_2} &= 2 \\
 C_{\alpha_1} &= 3, & C_{\alpha_3} &= -1 \\
 C_{\alpha_2} &= 2, & C_{\alpha_3} &= -1
 \end{aligned} \tag{8}$$

Since each of the pressure coefficients  $C_{\alpha_1}$ ,  $C_{\alpha_2}$ , and  $C_{\alpha_3}$  are equally valid, and since we need only two ( $C_\alpha$  and  $C_\beta$ ) to determine the angle of attack,  $\alpha$ , and the angle of sideslip,  $\beta$ , as is the case using a five-hole probe, we suggest a method to convert the  $C_{\alpha_1}$ ,  $C_{\alpha_2}$ , and  $C_{\alpha_3}$  coefficients to a  $C_\alpha$ ,  $C_\beta$  pair with a properly weighted combination of the three pressure coefficients. One should keep in mind that the three intersections described by Eqn. (4) may not be identical due to slight curvatures and nonlinear spacing of the lines in Figure 3, a complication which is not unique to seven-hole probes. Such curvatures also occur in five-hole calibrations. In short, the details of the intersection at the tail of the velocity vector might really appear as in Figure 4.

In the scheme that follows, the values of  $C_\alpha$  and  $C_\beta$  are selected by averaging the coordinates of the three intersections of the  $C_{\alpha_1}$ ,  $C_{\alpha_2}$ , and  $C_{\alpha_3}$  lines. This puts the final point at the centroid of a "triangle of confusion" shown in Figure 4 and removes redundancy.

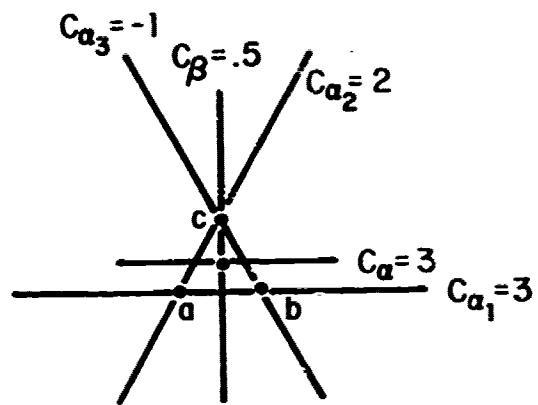


Figure 4. Details of Intersection

The equations of the  $C_{\alpha_1}$ ,  $C_{\alpha_2}$ , and  $C_{\alpha_3}$  lines are given respectively by:

$$C_{\alpha} = C_{\alpha_1} \quad (9)$$

$$C_{\alpha} = -C_{\beta} \tan 60^{\circ} + \frac{C_{\alpha_2}}{\sin 30^{\circ}} \quad (9)$$

$$C_{\alpha} = C_{\beta} \tan 60^{\circ} - \frac{C_{\alpha_3}}{\sin 30^{\circ}}$$

Eqns. (9) are three equations in the two unknowns  $C_{\alpha}$  and  $C_{\beta}$ , so three equally valid solutions are possible, each corresponding to an apex of the triangle shown in Figure 4.

$$\begin{pmatrix} 1 & 0 \\ 1 & \tan 60^{\circ} \end{pmatrix} \begin{pmatrix} C_{\alpha} \\ C_{\beta} \end{pmatrix}_a = \begin{pmatrix} C_{\alpha_1} \\ \frac{C_{\alpha_2}}{\sin 30^{\circ}} \end{pmatrix} \quad (10)$$

$$\begin{pmatrix} 1 & 0 \\ 1 & -\tan 60^{\circ} \end{pmatrix} \begin{pmatrix} C_{\alpha} \\ C_{\beta} \end{pmatrix}_b = \begin{pmatrix} C_{\alpha_1} \\ \frac{-C_{\alpha_3}}{\sin 30^{\circ}} \end{pmatrix} \quad (10)$$

$$\begin{pmatrix} 1 & \tan 60^{\circ} \\ 1 & -\tan 60^{\circ} \end{pmatrix} \begin{pmatrix} C_{\alpha} \\ C_{\beta} \end{pmatrix}_c = \begin{pmatrix} \frac{C_{\alpha_2}}{\sin 30^{\circ}} \\ \frac{-C_{\alpha_3}}{\sin 30^{\circ}} \end{pmatrix} \quad (10)$$

Eqns. (10) are solved for the  $C_\alpha$ 's and  $C_\beta$ 's in terms of  $C_{\alpha_1}$ ,  $C_{\alpha_2}$ , and  $C_{\alpha_3}$ . The values of  $C_\alpha$  and  $C_\beta$  are determined from the average of the three pairs:

$$C_\alpha = \frac{C_{\alpha_a} + C_{\alpha_b} + C_{\alpha_c}}{3} \quad C_\beta = \frac{C_{\beta_a} + C_{\beta_b} + C_{\beta_c}}{3} \quad (11)$$

The final result of the indicated algebraic operations is:

$$C_\beta = \frac{1}{\sqrt{3}} (C_{\alpha_2} + C_{\alpha_3}) \quad C_\alpha = C_{\alpha_1} + \frac{C_{\alpha_2} - C_{\alpha_3}}{2} \quad (12)$$

In summary, the process for getting a  $C_\alpha$  and  $C_\beta$  from the seven measured pressures of the seven-hole probe is to first substitute the pressures measured from the probe into Eqns. (6) to find  $C_{\alpha_1}$ ,  $C_{\alpha_2}$ , and  $C_{\alpha_3}$ , then substitute these pressure coefficients into Eqns. (12) to find  $C_\alpha$  and  $C_\beta$ . From this point on a determination of the angles would proceed exactly as in the case for the five-hole probes measuring at low flow angles (Ref. 1).

#### D. Division of Angular Space

If one follows the methods described above, the only remaining questions concern the determination of when to use the equations for low flow angles and when to use the equations for high flow angles. Associated with these questions is the task of specifying the dividing lines for each of the six 60-degree sectors when using the high flow angle equations. Initially, because of the experience with the five-hole probes, one is tempted to specify a 30-degree cone around the nose of the probe as the cut-off point for using the low flow angle equations. To do this, however, is naive since data taken during a survey of a known flow field (done for the purpose of calibrating the probe) may suggest a better cut-off angle and this will only be apparent after calibration. Further, arbitrarily locating the sector division lines might also prove naive after examining calibration data. Therefore, we suggest the plan shown schematically in Figure 5, which describes the decision network for deciding which angle pressure coefficient pair to use in determining the flow angles  $\alpha$  and  $\beta$ .

There are several commonly used reference systems for measuring the flow angle with respect to a probe axis at low flow angles. To select the angle description reference system that could best be adapted to a power series curve fit, we used the argument that the angle pressure coefficients  $C_\alpha$  and  $C_\beta$  should be unaffected by velocity components that are perpendicular to the plane in which the angles  $\alpha$  and  $\beta$  are measured. That is, the pressure coefficient  $C_\alpha$  which would be roughly proportional to  $\alpha$  in the chosen reference system would be nearly independent of  $\beta$  and vice versa. This argu-

ment leads to the selection of the tangent reference system which yields the angles  $\alpha_T$  and  $\beta_T$  shown in Figure 6.

For measuring at high flow angles, no conventional reference system is appropriate because they all have indeterminate angles and singularities at very high total flow angles. Therefore, for the high flow angles, we use the  $\theta, \phi$  method described earlier, which has a singular determination only when the velocity vector is aligned with the probe. This singularity is eliminated by switching to the low flow angle coordinate system.

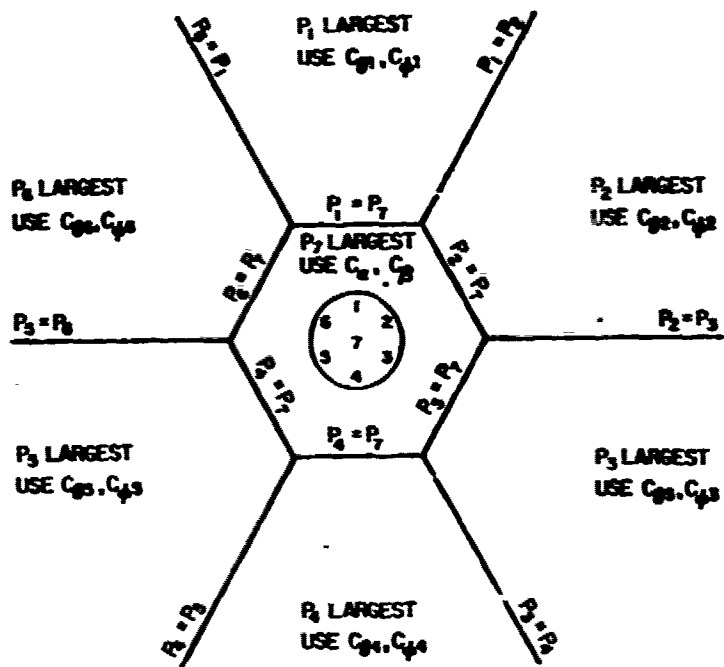
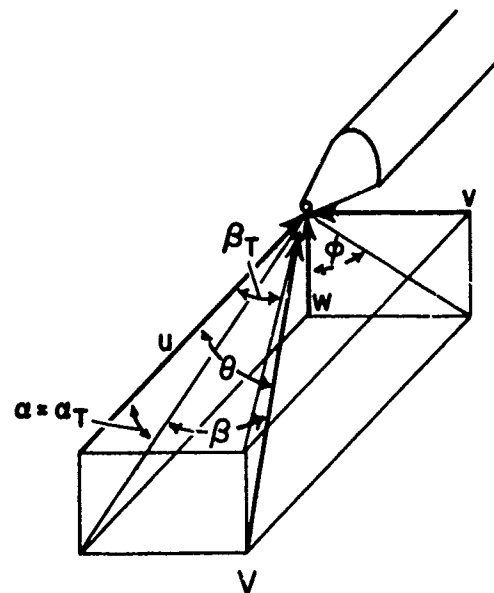


Figure 5. Division of Angular Space  
Based on Measured Pressures

Ideally, of course, the lines of constant  $C_a$ ,  $C_b$ ,  $C_\theta$ , and  $C_\phi$  in Figure 7 would be equally spaced and parallel to the lines of constant  $\alpha_T$ ,  $\beta_T$ ,  $\theta$  and  $\phi$  respectively. In reality, for a host of reasons, this is not exactly true. That is, the nominally constant calibration coefficients are not really constant and are more complicated than a simple linear relation. This complication is the topic of the following sections.

### III. Seven-Hole Probe Calibration Theory

At the beginning of the paper we mentioned that we wanted a method of measuring fluid flow properties that would yield the desired output quantities explicitly. Additionally, we insisted that the procedures necessary to perform a calibration of the probe to provide power series coefficients must be amenable to our available mechanical



CONVENTIONAL	POLAR	TANGENT
$u = V \cos \alpha \cos \beta$	$u = V \cos \theta$	$\alpha_T = \arctan \frac{w}{u}$
$v = V \sin \beta$	$v = V \sin \theta \sin \phi$	$\beta_T = \arctan \frac{v}{u}$
$w = V \sin \alpha \cos \beta$	$w = V \sin \theta \cos \phi$	

Figure 6. Flow Angle Definitions

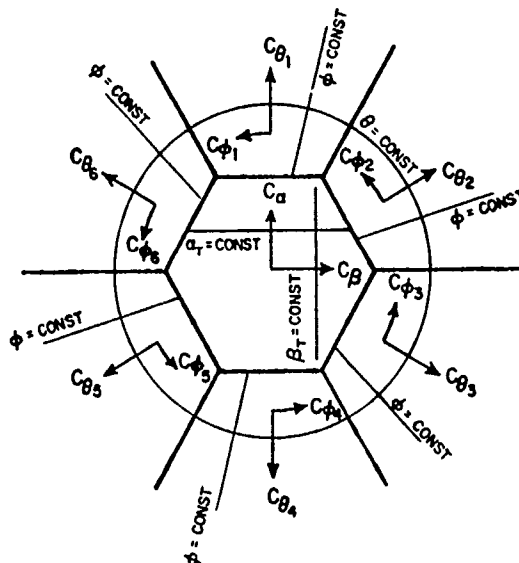


Figure 7. Idealized Coordinate Systems

apparatus could not require the development of extensive special-purpose computer software. We also wanted our calibration scheme to be capable of being extended to compressible flow situations. This section of the paper describes the mathematical structure and calibration of a power series determination method which meets all these requirements. By using this method we obtain a statistically correct estimate of the accuracy with which each measurement can be made.

#### A. Form of the Desired Flow Property Determination Method

In each of the seven regions of the flow around the probe (which are illustrated in Figure 5) the desired output quantities are represented by a power series in the pair of pressure coefficients most sensitive to the flow angles to be measured. Although there is some arbitrariness in specifying the form of the defining equations, we have found the following form can accurately reproduce the experimental data. For the inner sector (low flow angle) we define  $\alpha_T$ ,  $\beta_T$ , and  $C_o$  and  $C_q$  by these equations:

$$\begin{aligned} \alpha_T &= K_1^\alpha + K_2 C_\alpha + K_3 C_\beta + \dots \quad 0(4) \\ \beta_T &= K_1^\beta + K_2 C_\alpha + K_3 C_\beta + \dots \quad 0(4) \\ C_o &= K_1^o + K_2 C_\alpha + K_3 C_\beta + \dots \quad 0(4) \\ C_q &= K_1^q + K_2 C_\alpha + K_3 C_\beta + \dots \quad 0(4) \end{aligned} \quad (13)$$

For each outer region  $\theta_n$ 's and  $\phi_n$ 's,  $C_{\theta_n}$ 's and  $C_{\phi_n}$ 's are given by these equations:

$$\begin{aligned} \theta_n &= K_1^{\theta n} + K_2 C_{\theta n} + K_3 C_{\phi n} + \dots \quad 0(4) \\ \phi_n &= K_1^{\phi n} + K_2 C_{\theta n} + K_3 C_{\phi n} + \dots \quad 0(4) \\ C_{\theta n} &= K_1^{\theta n} + K_2 C_{\theta n} + K_3 C_{\phi n} + \dots \quad 0(4) \\ C_{\phi n} &= K_1^{\phi n} + K_2 C_{\theta n} + K_3 C_{\phi n} + \dots \quad 0(4) \end{aligned} \quad (14)$$

The K's are calibration coefficients. These are constant and unique to the particular probe. Assuming the K's are known, when taking data one uses the pressures measured on the probe to first determine which sector is appropriate (see Figure 5) and then to calculate the pair of angle pressure coefficients ( $C_\alpha$  and  $C_\beta$  or  $C_{\theta_n}$  and  $C_{\phi_n}$ ) appropriate to that sector by using Eqns. (13) or (14). We then have the two flow angles and the pressure coefficients  $C_o$  and  $C_q$  or  $C_{\theta_n}$  and  $C_{\phi_n}$ . Note that this information requires no iteration; we obtain it explicitly. The local dynamic pressure is then easily and explicitly obtained from  $C_q$  or  $C_{\phi_n}$  and the measured pressures. Further, the total pressure can be explicitly obtained from  $C_o$  or  $C_{\theta_n}$  and the measured pressures, as for example in the inner sector calculation shown below:

$$P_{oL} = P_7 - C_o (P_7 - \bar{P}_{1-6}) \quad (15)$$

$$P_{OL} - P_{\infty L} = \frac{P_7 - \bar{P}_{1-6}}{C_q} \quad (16)$$

As long as the flow being measured is incompressible, Eqns. (13), (14), (15) and (16) completely describe the steady component of the flow at a point. That is, it gives its angle referenced to the probe and the means to calculate the magnitude of the flow velocity. A characteristic advantage of pressure probes calibrated in this manner is that the local values of total and static pressure can be found. This is not the case when the hot wire and the laser doppler velocimeter methods are used. This method of measurement can also be extended to compressible fluid flows.

#### B. Calculating the Calibration Coefficients

If the two-variable power series are carried out to the fourth order, a complete probe calibration for measuring incompressible flow is possible but requires 420 calibration coefficients (four sets of fifteen for each of the seven regions). Because of the large number of calibration coefficients required, computer-based data acquisition systems are a necessity. While the mathematics of a complete set of equations for describing incompressible flows is cumbersome because the method is programmed in a high-level language using matrix notation, the actual programming is quite compact and streamlined. Netter (Ref. 7) described the matrix notation method for obtaining the calibration coefficients used for determining the angle of attack,  $\alpha$ . Similar relations can be found to find the calibration coefficients required for the polynomials representing the other desired output variables. To demonstrate the process for finding these calibration coefficients we start with the matrix  $R$  representing the pressure coefficient matrix for, in this case, the angle of attack polynomial. (Note that these pressure coefficients are, in a sense, output data from the probe, so at a known angle of attack  $\alpha_T$  the only unknowns are the  $K$ 's.)

$$R = \begin{bmatrix} 1 & C_{\alpha_1} & C_{\beta_1} & C_{\alpha_1}^2 & \dots & C_{\beta_1}^4 \\ 1 & C_{\alpha_2} & C_{\beta_2} & C_{\alpha_2}^2 & \dots & C_{\beta_2}^4 \\ \vdots & & & & & \\ 1 & C_{\alpha_m} & \dots & \dots & \dots & C_{\alpha_m}^4 \end{bmatrix} \quad (17)$$

In Eqn. (17), the subscript  $m$  is the number of data points being used to find the  $K$ 's of Eqn. (13) for a particular sector. Eqn. (13) may then be written in a matrix form and manipulated to yield an explicit relationship for the  $K$ 's in terms of  $\alpha_T$  and  $R$ .

$$[\alpha_T] = [R] [K^\alpha]$$

$$[R^T] [\alpha_T] = [R^T R] [K^\alpha] \quad (18)$$

$$[R^T R]^{-1} [R^T] [\alpha_T] = [R^T R]^{-1} [R^T R] [K^\alpha] = [K^\alpha]$$

The values of the K's result in a polynomial that best fits the data set in a least squares sense. Also, having found the K's, it is a simple matter to calculate an output quantity, say  $\alpha_T$ , corresponding to each of the pairs of coefficients, say  $C_\alpha$  and  $C_\beta$ , used in the computation of the K's and to compare these calculated output values to the experimental values. A global estimate of the accuracy of the curve fit (that is, the polynomial expression for each of the desired output quantities) can be obtained by computing the standard deviation of the difference between the experimental points and those predicted by the calibration polynomials. This standard deviation,  $\sigma_{(\alpha_T)}$ , is given by Eqn. (19):

$$\sigma_{(\alpha_T)} = \left[ \frac{\sum (\alpha_{T\text{EXP}} - \alpha_{T\text{POLY}})^2}{m} \right]^{\frac{1}{2}} \quad (19)$$

The discussion above applies to a probe angle of attack which falls in the inner sector (low flow angle) only. The same reasoning applies to the other three output variables obtained in the inner sector ( $\beta_T$ ,  $C_o$ ,  $C_q$ ) and to the four output variables obtained in each outer sector, (high flow angles).

While the standard deviations in the angles  $\alpha_T$  and  $\beta_T$  are representative of the accuracy with which these angles are calculated by the polynomials, the standard deviation in  $C_o$  and  $C_q$  are not representative of the accuracy of the obtained total pressure and dynamic pressure. The correct expressions for the standard deviation of these two latter coefficients are

$$\frac{\sigma(q)}{P_{oL} - P_{\infty L}} = \frac{\sigma(C_q)}{C_q}, \quad (20)$$

$$\frac{\sigma(P_{oL})}{P_{oL} - P_{\infty L}} = \left( (C_q \sigma(C_o))^2 + (C_o \sigma(C_q))^2 \right)^{\frac{1}{2}} \quad (21)$$

These expressions can be derived by the proper application of small perturbation analysis or by taking partial derivatives of the defining equations and subsequent application of the method of Kline and McClintock (Ref. 8).

### C. Extension to Compressible Flow

To understand how to extend these ideas to permit measurement of compressible fluid flows, first realize that the total and static pressure can be extracted from the method already described and thus the Mach number can be calculated by means of the following equation:

$$\frac{P_{oL} - P_{\infty L}}{P_{oL}} = \left( \frac{P_7 - \bar{P}_{1-6}}{C_q} \right) \frac{1}{P_7 - C_o (P_7 - \bar{P}_{1-6})} \quad (22)$$

and by:

$$M = \sqrt{\left(1 - \left(1 - \frac{P_{OL} - P_{\infty L}}{P_{OL}}\right)^{-\frac{\gamma-1}{\gamma}}\right) \frac{2}{\gamma-1}} \quad (23)$$

While we can make this calculation, a question arises as to whether or not this is the correct Mach number for high subsonic and supersonic flows. The accuracy of the computation can be checked by taking data for several known Mach numbers and comparing the calculated value with the actual value thereby obtaining proper corrected figures. This process leads to an iterative procedure, something an experimentalist tries to avoid.

An alternative method of calculating and checking the accuracy of measurements of compressible flow would be to extend the mathematical form of the method to include another pressure coefficient representative of compressibility. This additional pressure coefficient should be calculable from only the pressures measured on the probe. To satisfy the requirement that it is an extension of the incompressible method, the selected coefficient should go to zero at the small Mach numbers (zero Mach number limit). That is, the additional terms beyond those in the incompressible determination method should go to zero. Two possibilities for this coefficient are  $(P_7 - \bar{P}_{1-6})/\bar{P}_{1-6}$  and  $(P_7 - \bar{P}_{1-6})/P_7$ . A further requirement is that the selected pressure coefficient should approach some finite value in the hypersonic limit. This condition eliminates the coefficient  $(P_7 - \bar{P}_{1-6})/\bar{P}_{1-6}$  which goes to infinity at the hypersonic limit leaving us with the new pressure coefficient,  $C_M$ , as  $(P_7 - \bar{P}_{1-6})/P_7$ . The lower curve in Figure 8 shows an idealized variation of this pressure coefficient with Mach number. The result of adding  $C_M$  to

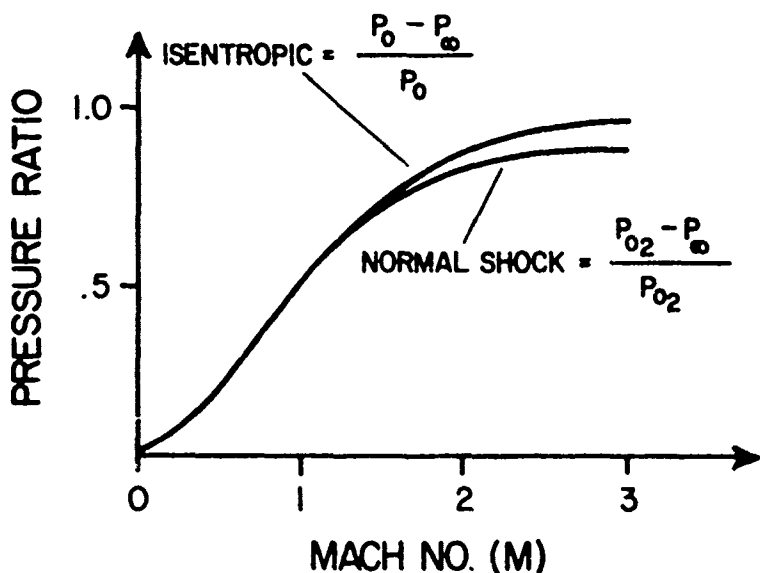


Figure 8. Pressure Ratios as Functions of Mach Number

the determination scheme is Eqn. (24):

$$\alpha = K_0 + K_1 C_\alpha + K_2 C_\beta + K_3 C_M + K_4 C_\alpha^2 + K_5 C_\beta^2 + K_6 C_M^2 + \\ K_7 C_\alpha C_\beta + K_8 C_\alpha C_M + K_9 C_\beta C_M + \dots \quad (24)$$

In the application of these calibrations we use the isentropic Eqn. (25)

$$\frac{P_{oL} - P_{\infty L}}{P_{oL}} = 1 - \left( 1 - \frac{\gamma-1}{2} M_L^2 \right)^{-\frac{\gamma}{\gamma-1}} \quad (25)$$

to calculate the Mach number when it is less than one (subsonic) corresponding to the pressure ratio

$$\frac{P_{oL} - P_{\infty L}}{P_o} < .472$$

And we use the Rayleigh-Pitot formula below

$$\frac{P_{oL} - P_{\infty L}}{P_{oL}} = 1 - \frac{\left( \frac{2\gamma}{\gamma+1} M_L^2 - \frac{\gamma-1}{\gamma+1} \right)^{\frac{1}{\gamma-1}}}{\left( \frac{\gamma+1}{2} M_L^2 \right)^{\frac{\gamma}{\gamma-1}}} \quad (26)$$

to calculate the Mach number if the flow is supersonic corresponding to the pressure ratio

$$\frac{P_{oL} - P_{\infty L}}{P_o} > .472$$

The total pressure,  $P_{oL}$ , in Eqn. (26) is the total pressure behind a normal shock wave. Here, for supersonic flows, the total pressure indicated by the determination scheme will be very nearly the total pressure behind a normal shock wave. The static pressure indicated by the probe determination method will be near the free stream static pressure in both subsonic and supersonic flow. Also,  $(P_{oL} - P_{\infty L})/P_{oL}$  is approximated by  $(P_7 - \bar{P}_{1-6})/P_7$  and at a minimum we would expect them to be nearly linear functions of each other. Therefore, the polynomials are not required to fit the compressible flow relations of Eqns. (25) and (26). Because of the unpredictable nature of transonic flow, this scheme may not yield good data near the speed of sound but should yield good results at all other Mach numbers. As the hypersonic limit is approached, the Mach number becomes irrelevant and cannot be calculated by any pressure probe method.

A complete compressible calibration of a probe in this manner requires that a range of Mach numbers be tested. However, as in the case of angle of attack and angle of

sideslip variations, it is not necessary to take complete sets of data at each specific Mach number. Instead, one simply has to insure that the entire parameter space (angle of attack, angle of sideslip, and Mach number) is roughly uniformly covered by a data set that has a number of points that exceeds the number of calibration coefficients ( $K$ 's) to be found in each series by about 20 to allow an accurate calculation of a standard deviation.

#### IV. Apparatus and Procedures for Calibration

This section describes how we make our probes, the various stings and holders used in calibration, the sequential calibration procedure, and the associated software.

##### A. Probe Manufacture

The manufacturing technique used for building the seven-hole probe is quite similar to the one used for the five-hole probes (Ref. 9). The seven-hole probe is somewhat simpler because the seven properly-sized tubes can only be packed into the outer tube in a unique way as shown in Figure 9. This design eliminates the need to find properly-

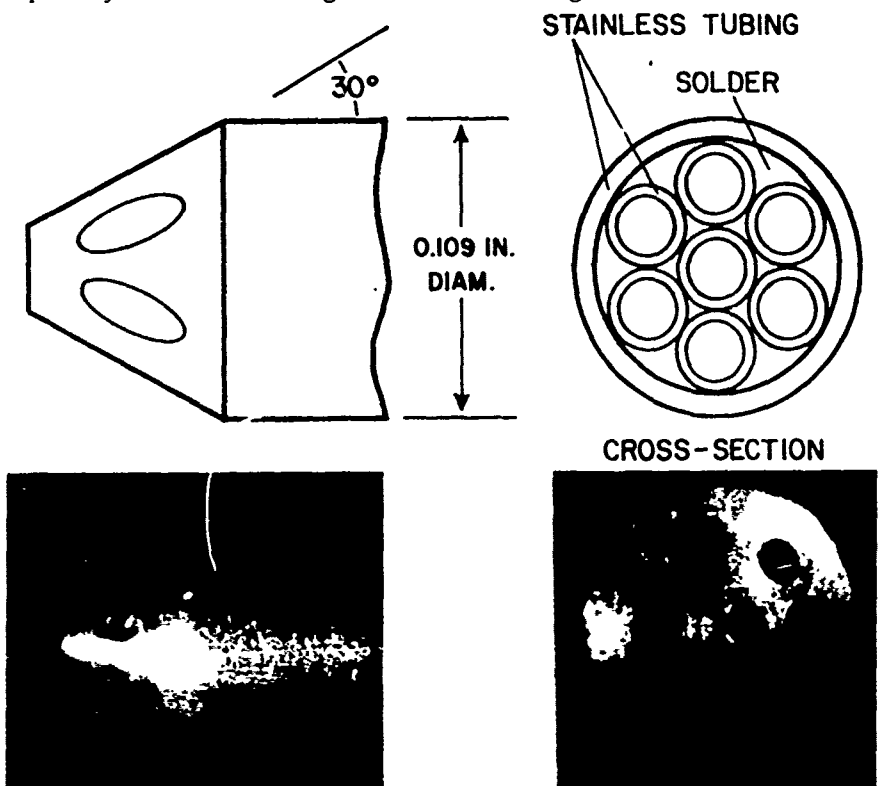


Figure 9. Probe Tip Geometry

sized spacers which are required in the manufacture of five-hole probes (Ref. 9). Another refinement is that we now machine the conical surface of the probe with a very sharp tool that has generous relief angles. This technique permits smooth cutting through the alternately hard and soft materials which form the probe. Otherwise the technique is the same

as that described for the five-hole probes. That is, in the end the seven-hole probe retains the advantage of large flow areas in a probe of given diameter.

#### B. Mechanical Set-Up for Calibration

For total flow angles of less than 30 degrees, we mount the probe on a conventional wind tunnel sting holder. The same mechanism that is used for changing the angle of attack of sting-mounted models is used to sweep the probe through an angle of attack range of -30 to +30 degrees. By rolling the probe in its holder, we can repeat the sweep to obtain sideslip angles. An important feature of the calibration scheme is that the data does not have to be taken along lines of constant angle of attack or lines of constant angle of sideslip. Consequently, the probe is set at a constant roll angle and total angle sweeps are used.

For total flow angles between 30 and 90 degrees, we use the bent sting arrangement shown in Figure 10. Again, roll angles are set by rolling the probe about its own

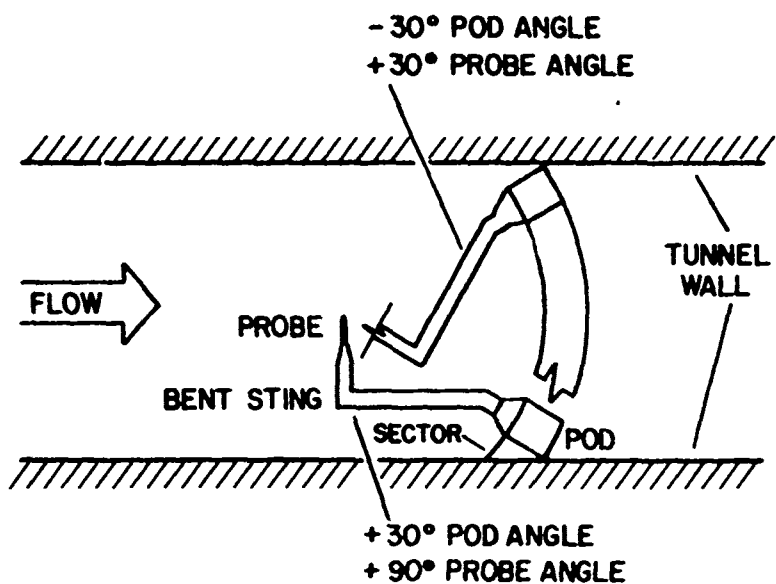


Figure 10. Bent Sting Geometry

axis and sweeping the angle of attack.

Frequently, for some of the data taken on the straight sting, one of the outer pressures will be greater than the pressure at hole number seven. When this situation occurs it signals that the probe has entered a high flow angle region and the data is properly sorted into the correct sector by our computer program. The program also provides for the case where some of the data taken on the bent sting should properly fall into the low angle region. Figure 11 shows a simplified schematic and wiring diagram of the experimental set-up for running calibration tests. The sequence of operations and the functions of the various software packages is described below.

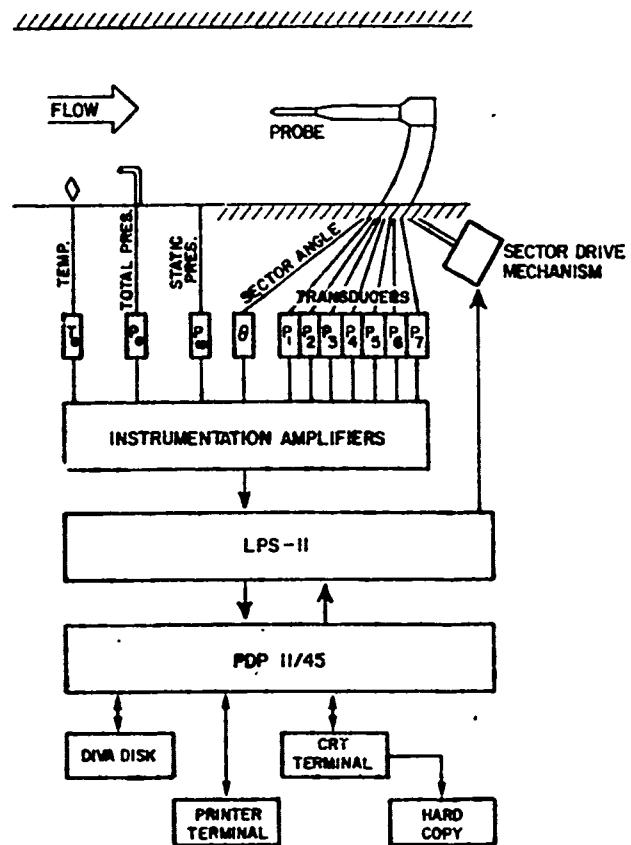


Figure 11. Apparatus Arrangement for Calibration

### C. Procedure and Software

The procedures are directed by the software package so that the entire process is automated. The software is made up of several pieces, each of which has its own title and is referred to by name in this description. The driver part of the software first calls for and records a representative set of data that roughly evenly covers the  $2\pi$  steridian angular space containing the velocity vector. This data is recorded (stored) in a file where it is held for sorting into sectors by the highest pressure. After sorting, the data for each sector is used to calculate the calibration coefficients (K's) for that particular sector. The following paragraphs describe each of these steps in some detail.

After the probe is installed and properly leveled on the sting, a program in the software package titled SHP moves the sting and takes the data. Required operator inputs for this phase include information about the sting being used and the roll angle of the probe. The computer automatically selects the specific locations for data acquisition shown in Figure 12 and it samples the data at these locations. This process must be repeated for both the straight and bent stings to complete the calibration of the probe. After each angle of attack,  $\alpha$ , the wind tunnel is stopped and the probe is positioned

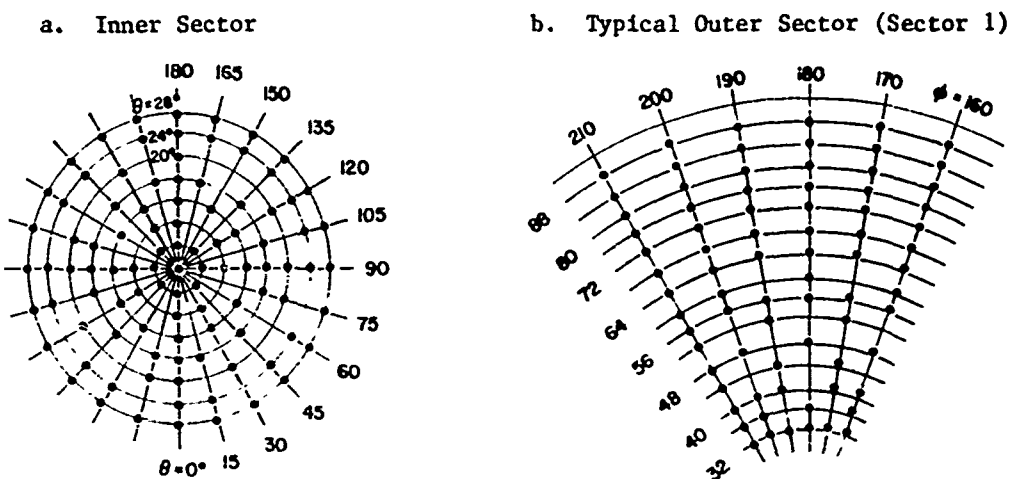


Figure 12. Distribution of Points Over Angular Space

to a new roll angle. Currently, only the roll angles shown in Figure 12 can be used since the computer program decides which angles to stop at based on these input roll angles. For each data point, this program stores the absolute pressure at each port, the roll angle, the total angle of attack, the tunnel total and static pressures, and the tunnel temperature.

The next program, titled SORT, sorts the data into sectors based on the highest pressure. There is no way of knowing how many data points will fall in each sector. One must verify that enough points have fallen in each sector to provide a reasonable calibration. Also, to perform the subsequently required matrix operations, the exact number of points in each sector must be known to properly describe the size of the R matrix to be used. To accomplish this matrix operation we currently have to modify another computer program, although there is no reason that this task could not be avoided by using a more capable system in the computer for handling matrices. Our current program also calculates the pressure coefficients  $C_\alpha$ ,  $C_\beta$  or  $C_\theta$ ,  $C_\phi$ .

The calibration coefficients (K's) are then calculated for each sector in turn by programs called K1 through K7 using the matrix equations already described. The number of data points in each sector is required to write dimension statements for each of these programs. Additionally, this program substitutes the actual pressures into the calibration polynomials at each data point and determines the output variable that would have been calculated by the polynomial for that point. The difference between this and the actual output variable is an error in the calibration curve. The computer program sums the squares of these errors and divides the sum by the number of data points in that sector and takes the square root to find the standard deviation of the data set. This standard deviation provides an excellent assessment of the curve fit and the overall accuracy achieved. Four standard deviations are computed for each of the seven sectors, one for each of the two angles, one for the total pressure coefficient, and one for the dynamic pressure

coefficient.

This completes the calibration of a probe for measuring incompressible flows.

#### V. Examples

We have calibrated two probes so far, each with a slightly different nose shape. The results were quite similar and few conclusions can be drawn from the differences in calibrations. Therefore, in this section we will discuss the common features of both calibrations which seem to be characteristic of this type of probe.

The probe geometry tested is shown in Figure 9. The only difference between the two shapes is the conical angle: 25 degrees for one and 30 degrees for the other. The general features of the low angle calibration are shown in Figures 13, 14 and 15. Figure 13 depicts lines of constant  $C_\alpha$  and constant  $C_\beta$ . If these coefficients were linearly dependent on their respective angles, and independent of the other angle, this figure would appear as evenly-spaced horizontal and vertical lines. The relative lack of orthogonality and any unevenness in spacing indicates deviation from this ideal behavior. Manufacturing assymmetries or fluid mechanical effects overlooked in our simplified model of flow around the probe are included in the curve fit. In any case, the fit is very good as indicated by the standard deviations of the attual angle data away from the calibration curves in the inner sectors tabulated in Table 1.

The lines of constant  $C_\alpha$  and constant  $C_\beta$  shown in Figures 14 and 15 generally behave as one would expect. First, we see that the total pressure is not properly measured by hole number seven at the higher angles. Specifically, the pressure measured at hole number seven is less than the true total at significant angles. However, the calibration

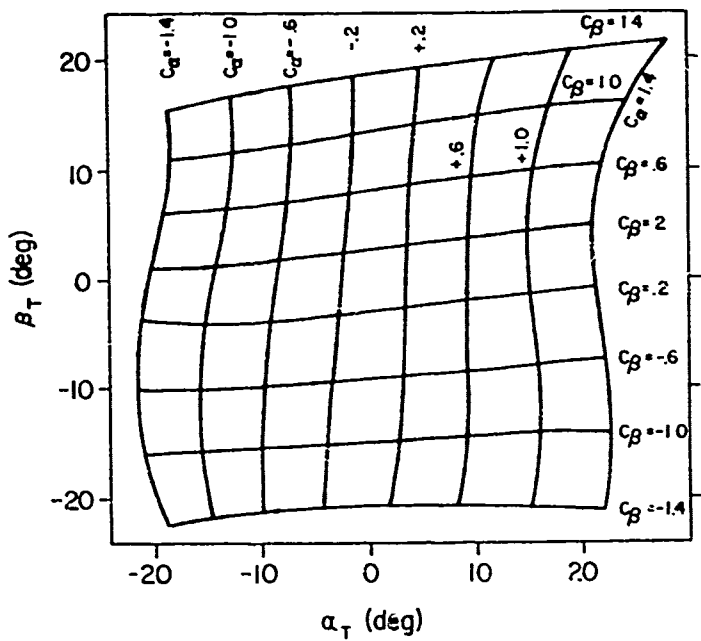


Figure 13.  $C_\alpha$  and  $C_\beta$  versus  $\alpha_T$  and  $\beta_T$  for Low Angles

Table 1  
STANDARD DEVIATIONS

AVERAGE OF TWO INNER SECTORS		AVERAGE OF 12 OUTER SECTORS	
Variable	Std. Dev.	Variable	Std. Dev.
$\alpha_T$	0.42°	$\theta$	0.84°
$\gamma$	0.36°	$\phi$	1.17°
$C_o$	1.0%	$C_{o_n}$	1.1%
$C_q$	0.6%	$C_{q_n}$	2.4%
$\frac{\sigma(P_{oL})}{P_{oL} - P_{\infty L}}$	0.6%	$\frac{\sigma(P_{oL})}{P_{oL} - P_{\infty L}}$	1.2%
$\frac{\sigma_q}{P_{oL} - P_{\infty L}}$	1.0%	$\frac{\sigma_q}{P_{oL} - P_{\infty L}}$	2.4%

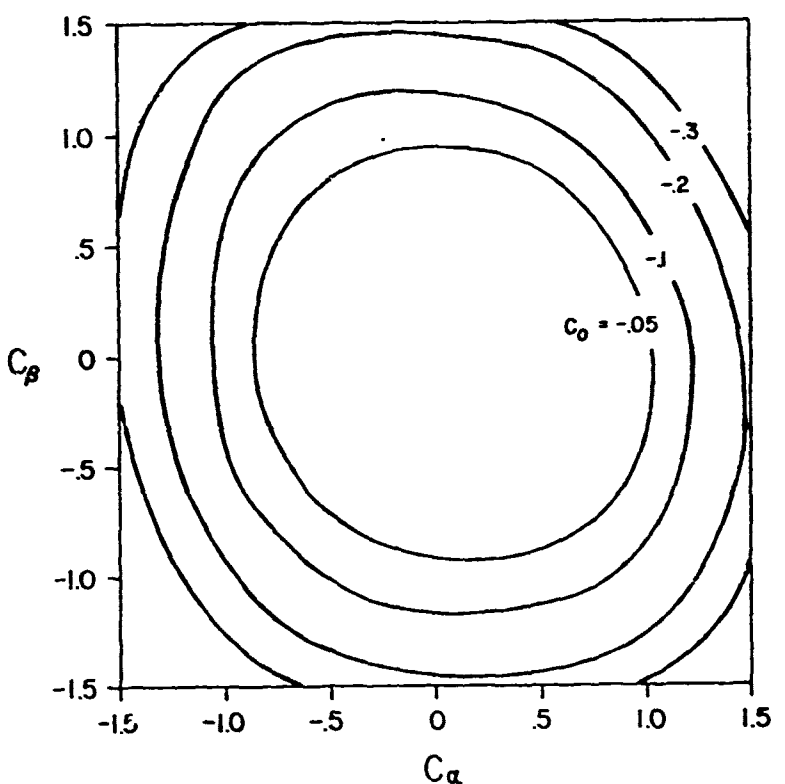


Figure 14. Coefficient  $C_o$  versus  $C_\alpha$  and  $C_\beta$  for Typical Inner Sector (30-Degree Nose Angle, Sector #7)

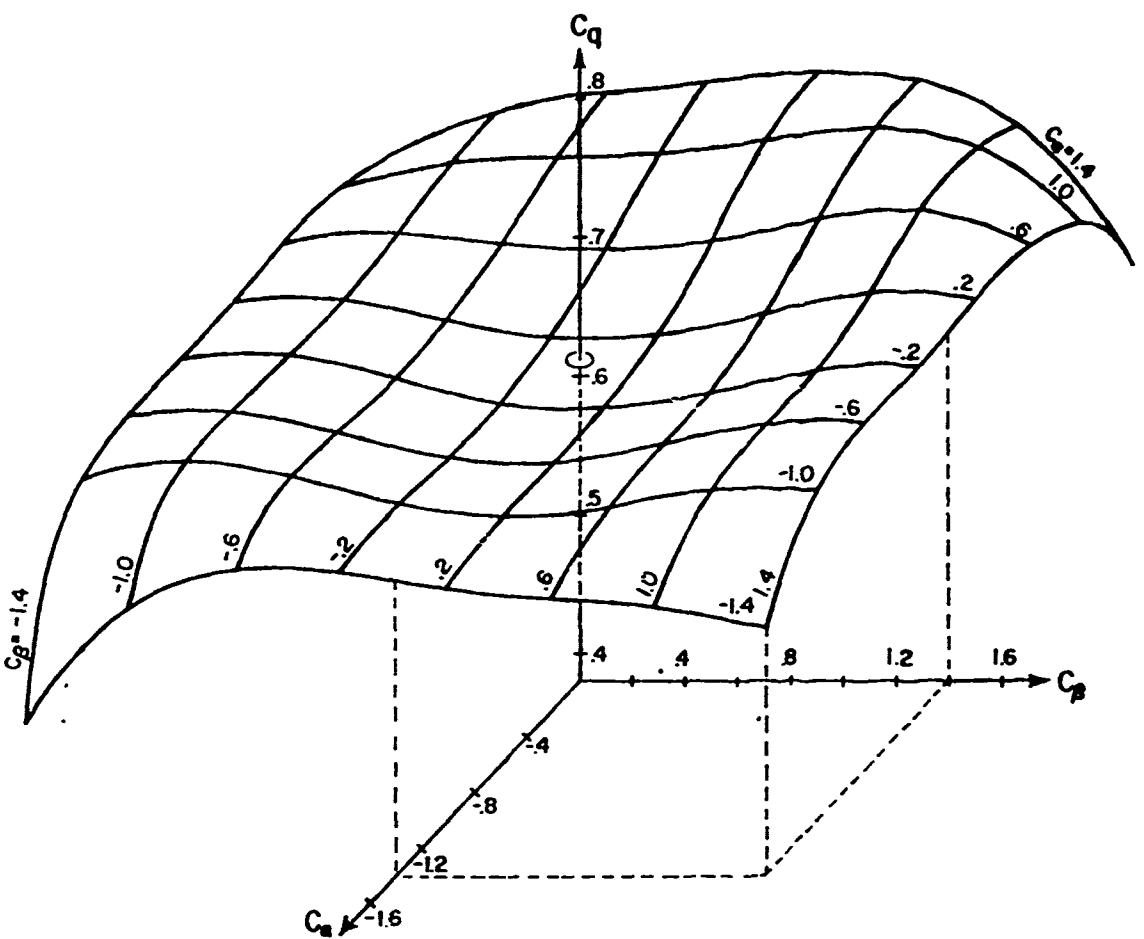


Figure 15. Coefficient  $C_d$  versus  $C_a$  and  $C_B$  for Inner Sector  
(30-Degree Nose Angle, Sector #7)

curves accurately correct for this effect as indicated by the low standard deviation of the coefficient  $C_d$  shown in Table 1. Similar features appear in Figure 15 depicting the dynamic pressure coefficient. The dynamic pressure approximated from the probe pressures by the differences between hole seven and the average of the outside six is less than the true dynamic pressure. This deficiency increases in an irregular way as the angle the flow makes with the probe axis increases. Again, the calibration curves account for this as indicated by the low value of the standard deviation shown in Table 1.

In test situations where the flow is at high angles, the features of the calibrations are much more interesting and reveal the final limitations to a determination method of this type. Consider the plot of  $C_{d,n}$  versus  $\theta$  shown in Figure 16. This is essentially raw data and it indicates why the calibration must be truncated at some point short of a total angle of 90 degrees. The curve has the general characteristic of the lift curve of a gently stalling airfoil. Apparently the reason for this behavior is that the pressure at hole seven continues to decrease with flow angle until it reaches a pressure quite a bit below a

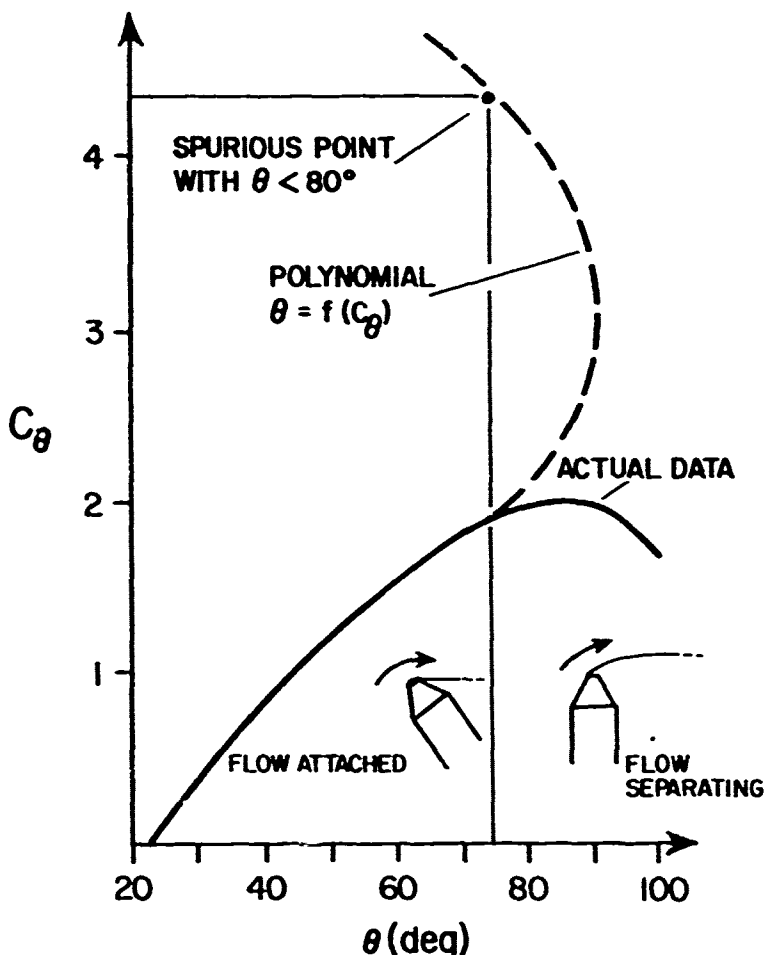


Figure 16. Final Limitation on Angular Range

free stream static condition. Then as the flow angle increases further, the suction on the tip of the probe disappears. A possible mechanism for the disappearance of the suction is indicated in Figure 16. In any case, data past the peak in this curve cannot be used because a single pressure coefficient corresponds to two possible angles of attack. Another feature of the determination scheme is that the polynomials giving desired flow properties cannot represent the curve past the peak because it is a polynomial in  $C_\theta$  not  $\theta$ . This feature is shown in Figure 16 as well. Because of this fundamental limitation, we have chosen to truncate our data sets to angles of less than 80 degrees. The lowest peak we have encountered occurs at 86 degrees. We are currently considering a revision of this procedure which would reject data where  $C_\theta$  or  $C_\delta$  exceeded a certain value. Such a policy would have value in the taking of data where data could be rejected before  $\theta$  was calculated. An additional advantage in basing the decision to reject data on the pressure coefficient is that no spurious calculations of angles could creep in that may appear completely valid. How this could happen is shown by the spurious point in Figure 16.

Other than the angular limitations mentioned above, the calibration curves for a typ-

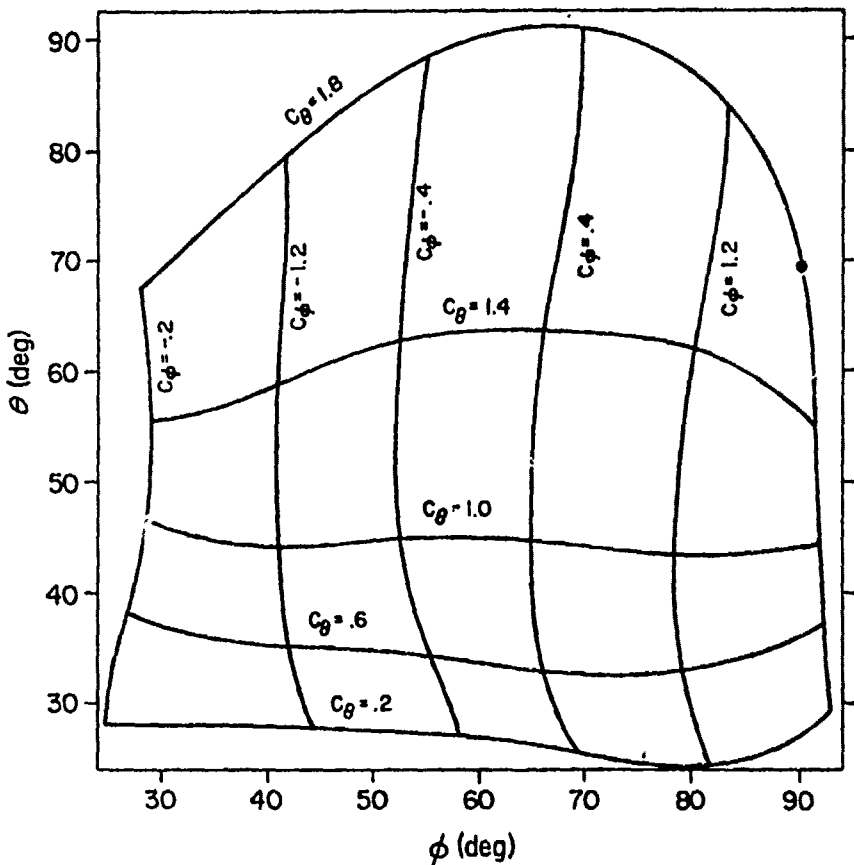


Figure 17.  $C_{\theta_3}$  and  $C_{\phi_3}$  versus  $\theta$  and  $\phi$  for a Typical High Angle Sector  
(30-Degree Nose Angle, Sector #3)

ical outer sector look quite similar to those for the inner sector. Figure 17 shows the angle coefficients,  $C_\theta$  and  $C_\phi$ , versus the flow angles,  $\theta$  and  $\phi$ . Again, the general feature of orthogonality and linear spacing is evident. However, it is clear that the polynomials are working harder to fit this data than in the low-angle sector. This is also shown by the standard deviations shown in Table 1 which are considerably larger than in the inner sector. Apparently there is a trade-off here. And apparently this lack of fit is related to the nonlinearity of the  $C_\theta$  versus  $\theta$  curve. If one was interested in measuring angles up to only 60 degrees, then a much closer fit would be possible. Figures 18 and 19 show the total pressure coefficient and the dynamic pressure coefficient respectively. Again, the features are not surprising. The windward hole only senses true total pressure at one specific angle, and the pressure sensed by this windward hole is less at all other angles. Similar features appear in the dynamic pressure coefficient. The standard deviations again reflect the difficulty of fitting the data in these outer sectors. The resulting accuracy is certainly adequate for most wind tunnel work. The remaining errors are not exclusively due to the determination method. These errors include transducer drifts and the mechanical inaccuracies associated with positioning the probe in the tunnel.

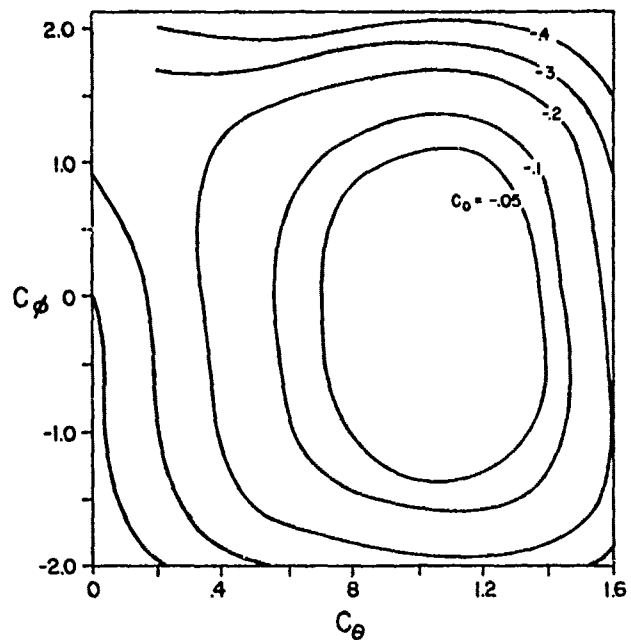


Figure 18. Coefficient  $C_{\phi}$  versus  $C_{\theta_n}$  and  $C_{\phi_n}$  for a Typical Outer Sector  
(30-Degree Nose Angle, Sector #2)

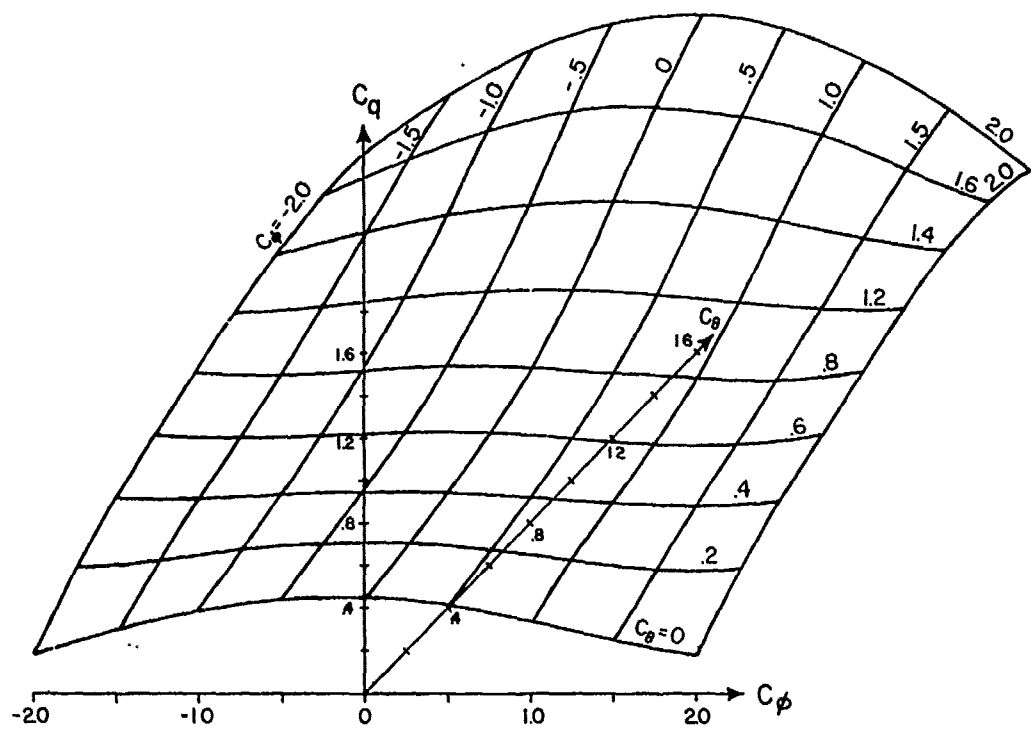


Figure 19. Coefficient  $C_{q_2}$  versus  $C_{\theta_2}$  and  $C_{\phi_2}$  for a Typical Outer Sector  
(30-Degree Nose Angle, Sector #7)

VI. Conclusions

We have described the manufacture, calibration, and use of a unique seven-hole probe that permits the accurate measurement of all steady flow properties provided that the local flow makes an angle of no more than 80 degrees with respect to the probe axis. This large angle capability exceeds, by at least a factor of two, the performance of the best probes of other designs. The determination method is comprised of explicit polynomial relations for all the desired output quantities in terms of pressures measured on the probe. This method is easily programmed in matrix notation on a modern and capable data acquisition system and does not require that the probe be tested at constant angles of sideslip or constant angles of attack as required by some other determination methods. Flexibility in the calibration procedure means that quite simple mechanical apparatus may be used in the calibration process. Once the calibration coefficients are determined by the calibration process, the determination method can be reapplied to the calibration data to obtain a statistical estimate of the expected error in the variables determined from the polynomials of the determination method. This expected error includes error from all possible sources.

We have also presented a method for extending the calibration to compressible flows both below and above the speed of sound, although no examples of such a calibration have yet been completed. Representative flow angle errors are .4 degrees at low flow angles and 1 degree at high flow angles. Expected errors in dynamic pressure are 1.0 percent at low flow angles and 2 percent at high flow angles.

VII. Acknowledgements

The design of this pressure probe measuring technique is the result of the coordinated efforts of a number of people. It depended on expert skills in mechanical design and manufacture, computer-experiment interface design, instrumentation, wind tunnel operation, and expert computer programming. Mr. Claude Hollenbaugh carefully constructed many of the small probes and the holding and indexing apparatus. Lt Ken Barker initially wrote much of the programming for calibration of the five-hole probe. This programming was later extended to the seven-hole probe design by Capt Tom Bolick. Two Air Force Academy student groups exercised the software on two different probes to assure that all the software worked properly. Additionally, Capt Bolick assisted the two cadet groups by troubleshooting the programs during each calibration to refine it to its present well-documented and efficient form. Mr. Charles Meadows operated the wind tunnel and the data acquisition system to acquire and reduce the massive amount of data needed to do a complete probe calibration.

NASA's Ames Research Center supported the effort as a step toward the goal of describing the flow around canard-configured aircraft at high angles of attack.

Symbols

$$C_o = \frac{P_7 - P_{oL}}{P_7 - \bar{P}_{1-6}}$$

apparent total pressure coefficient for low angles

$$C_{on} = \frac{P_n - P_{oL}}{P_n - \frac{P_{n+1} + P_{n-1}}{2}}$$

$$n = 1---6$$

$$n+1=1---6$$

$$n-1=1---6$$

apparent total pressure coefficients for high angles\*

$$C_q = \frac{P_7 - P_{1-6}}{P_{oL} - P_{\infty L}}$$

apparent dynamic pressure coefficient for low angles

$$C_{qn} = \frac{P_n - (P_{n+1} + P_{n-1})/2}{P_{oL} - P_{\infty L}}$$

$$n = 1---6$$

$$n+1=1---6$$

$$n-1=1---6$$

apparent dynamic pressure coefficient for high angles\*

$C_\alpha$

angle of attack pressure coefficient for low angles

$C_\beta$

angle of sideslip pressure coefficient for low angles

$C_{\theta n}$

total angle coefficient for high angles

$C_p$

roll angle coefficient for high angles

K

coefficient in power series (Superscript indicates variable being expanded. First digit of subscript indicates position in series. Second digit of subscript indicates one of six high angle sectors.)

$P_n$ ,  $n = 1---7$

pressure at port "n"

$\bar{P}_{1-6}$

average of pressures 1 through 6

$P_{oL}$

local total pressure

$P_{\infty L}$

local static pressure

$P_{o\infty}$

total pressure of free stream

\* $n = 1$  indicates the next hole clockwise from the  $n$  hole and  $n - 1$  indicates the next hole counterclockwise from the  $n$  hole as viewed from the front of the probe

$P_{\infty}$	static pressure of free stream
$U, V, W$	local velocity components with respect to probe
$\alpha_T$	angle between probe axis and velocity vector projected on vertical plane through probe axis
$\beta_T$	angle between probe axis and velocity vector projected on horizontal plane through probe axis
$\theta$	total angle between velocity vector and probe axis
$\varphi$	angle between a plane containing the velocity vector and probe axis and a vertical plane through the probe axis measured positive clockwise from port number four as viewed from the front'
$\sigma(\alpha_T)$	standard deviation of experimental values of $\alpha_T$ away from those calculated from the calibration expressions
$\sigma(\beta_T)$	standard deviation of angle of sideslip
$\sigma(q)$	standard deviation of dynamic pressure
$\sigma(C_q)$	standard deviation of coefficient $C_q$
$\sigma(C_o)$	standard deviation of coefficient $C_o$
$\sigma(p_{oL})$	standard deviation of total pressure

References

1. Barker, K., R. W. Gallington, and S. Minster. "Calibration of Five-Hole Probes for On-line Data Reduction." Aeronautics Digest - Spring 1979, USAFA-TR-79-7, USAF Academy, Colorado, July 1979.
2. Wuest, W. "Measurement of Flow Speed and Flow Direction by Aerodynamic Probes and Vanes." Paper presented at the 30th Flight Mechanics Panel Meeting, Montreal, Canada, 1967.
3. Huffman, G. D. "Calibration of Tri-Axial Hot Wire Probes Using a Numerical Search Algorithm." Aeronautics Digest - Fall 1979, USAFA-TR-80-7, USAF Academy, Colorado, April 1980.
4. Sforza, P. M. and M. J. Smorto. "Streamwise Development of the Flow Over a Delta Wing." AIAA Paper 80-0200, January 1980.
5. Reed, T. D., T. C. Pope, and J. M. Cooksey. "Calibration of Transonic and Supersonic Wind Tunnels." NASA Contractor Report 2920, Appendix II, November 1977.
6. Breyer, D. W. and R. C. Pankhurst. "Pressure-Probe Methods for Determining Wind Speed and Direction." London: Her Majesty's Stationery Office, 1971.
7. Netter, J. and W. Wasserman. Applied Linear Statistical Models. Homewood, IL: Richard D. Irwin, Inc., 1974.
8. Kline, S. J. and F. A. McClintock. "Describing Uncertainties in Single-Sample Experiments." Mechanical Engineering, January 1953.
9. Gallington, R. W. and C. F. Hollenbaugh. "A Fast Method for Accurate Manufacture of Small Five-Hole Probes." Aeronautics Digest - Spring 1979, USAFA-TR-79-7, USAF Academy, Colorado, July 1979.

## CANARD WAKE MEASUREMENT AND DESCRIPTION

C. Sisson\* and R. Crandall\*\*

### Abstract

This paper describes a method for measuring, describing, and visualizing the complex flow fields that occur when canard-configured aircraft models are tested in the wind tunnel. This simple, rapid, and inexpensive technique is a source of complex empirical aerodynamic data suitable for the preliminary design of future fighter aircraft. The technique makes use of a miniature seven-hole probe, a computer-driven traverse mechanism, computerized data acquisition equipment, and computer graphic displays. Numerical and graphic descriptions of wakes from three canard models are presented.

### I. Introduction

Since the summer of 1978 the U.S. Air Force Academy and NASA's Ames Research Center have participated in a joint research effort to understand the aerodynamics of canard-equipped aircraft. These configurations are similar to proposed fighter aircraft designs for the 1990's, which have pitch control surfaces located in front of the wings in lieu of a conventional aft-located tail. The program began as summer research projects, with Academy cadets and officers attempting to analytically predict the aerodynamics of these configurations using potential flow computer analysis. Their efforts were largely unsuccessful because the location of the canard wake was not known in advance. To solve this problem, NASA Ames contracted the USAF Academy Department of Aeronautics to develop a rapid, inexpensive technique to precisely measure the location of canard wakes.

The approach taken used specially-designed seven-hole pressure probes to collect pressure measurements in the model wake. One characteristic of canard wakes is a region of lower fluid-mechanical energy seen as a drop in total pressure. This wake exists at each point in the airstream where the measured total pressure differs significantly from the free-stream value. This region is located by placing the pressure-measuring probe at many points downstream of the model using a three-dimensional positioning mechanism known as a traverse. The measured pressures were plotted as contour graphs, where the steep pressure gradients (like those occurring at the edge of the canard wake) were indicated by a collection of closely-spaced contour lines. A series of these graphs compose a mapping of the flow field.

This entire procedure was reduced to four computer programs run in sequence. Each program prompts the computer operator for all necessary information. The time and expense required to perform the procedure is primarily a function of the three-dimensional traverse mechanism and how quickly it can move the pressure-measuring probe. The reduction and display of the data takes less than two additional minutes after data collection is complete. The procedure has been successfully performed by many Academy cadets and

\*Captain, USAF, Department of Aeronautics, DFAN

\*\*2nd Lieutenant, USAF, Department of Aeronautics, DFAN

officers on a variety of aerodynamic models. On the basis of these results the research can be considered successful in developing a new technique which can simply, rapidly, and inexpensively measure and describe the wakes of wind tunnel aerodynamic models.

This paper consists of four parts: (1) a theory section describing the expected results of mapping a theoretical vortex in the free-stream direction, (2) an apparatus description, (3) a procedure description, and (4) a discussion of the results of mapping three canard wakes. An appendix consisting of the user manual for the four computer programs is included.

## II. Theory

One of the simplest pieces of instrumentation for studying steady flow field properties is the pressure probe. It is easy to understand and manufacture, its use is widespread, and it directly measures one of the most important aerodynamic properties. The seven-hole pressure probe extends these characteristics to include direct measurement of local flow angles and static, total and dynamic pressure, and allows calculation of local velocities at angles up to 80 degrees off axis without iteration (Ref. 1). These properties make the seven-hole probe the best instrumentation for this research.

Total pressure is a measure of total fluid-mechanical energy and results from slowing the fluid velocity to zero without loss. Static pressure is the pressure exerted on an aerodynamic surface parallel to the free stream. Dynamic pressure is total pressure minus static pressure. All three pressures can be used to locate the canard wake by observing where large changes or gradients exist in the flow. Since these pressures are affected by slight changes in wind tunnel velocity or room temperature, pressure coefficients will be used instead, where the differences in local pressures and reference pressures are divided by tunnel dynamic pressure, resulting in:

$$\frac{\text{Static Pressure}}{\text{Dynamic Pressure}} = C_{\text{STATIC}} = \frac{P_{\infty L} - P_{\infty}}{P_0 - P_{\infty}}$$

$$\frac{\text{Total Pressure}}{\text{Dynamic Pressure}} = C_{\text{TOTAL}} = \frac{P_{\infty L} - P_0}{P_0 - P_{\infty}}$$

where

$P_{\infty L}$  = Local Static Pressure (measured by probe flow)

$P_{\infty}$  = Free Stream Static Pressure

$P_{\infty L}$  = Local Total Pressure (measured by probe in flow)

$P_0$  = Free Stream Total Pressure

To anticipate what our coefficients will resemble in the canard wake, we will start with a simpler example of an ideal two-dimensional vortex (Ref. 2). In an ideal two-dimensional vortex, angular velocity increases exponentially as the distance to the vortex filament (radius) decreases. (Figure 1). In reality the viscosity of the fluid reduces

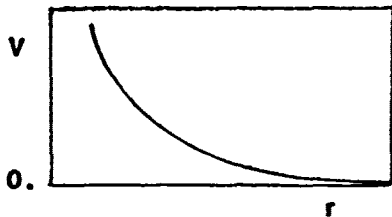


Figure 1. Fluid Velocity Versus Distance from Vortex Center for an Ideal Vortex

the angular velocity long before it reaches infinity (Ref. 3). In this region where viscous effects are substantial, the angular velocity drops until it is zero at the vortex center. Figure 2 shows the velocity distribution of a vortex with a viscous core

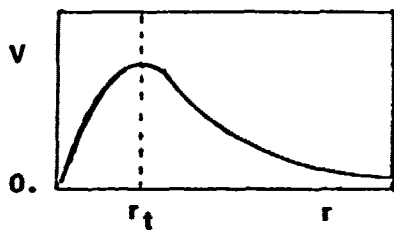


Figure 2. Fluid Velocity Versus Distance from Vortex Center for a Real Fluid

(Ref. 3). At distances greater than  $r_t$ , the flow is approximately inviscid.

The conventional aerodynamic pressure coefficient is defined as

$$C_{p_A} = \frac{P_A - P_\infty}{\frac{1}{2} \rho_\infty V_\infty^2},$$

where  $P_A$  is local static pressure at any Point A. In a steady, incompressible flow we have

$$\frac{1}{2} \rho_\infty V_\infty^2 = P_0 - P_\infty,$$

and then

$$C_{\text{STATIC}} = \frac{P_\infty L - P_\infty}{P_0 - P_\infty} = \frac{P_\infty L - P_\infty}{\frac{1}{2} \rho_\infty V_\infty^2},$$

which yields

$$C_{\text{STATIC}} = C_{p_A}.$$

$C_p$  is also defined by

$$C_p = 1 - \left( \frac{V_L}{V_\infty} \right)^2.$$

Since the conditions at infinity approach free-stream conditions,  $C_p$  and  $C_{\text{STATIC}}$  approach zero. As the radius decreases from infinity to  $r_t$ , the angular velocity increases. This

increase in velocity causes the static pressure to drop. Hence, as we go from  $r_\infty$  to  $r_t$ ,  $C_{\text{STATIC}}$  goes from zero to a negative value.

Out to  $r_t$ , viscous effects preclude the use of the previous equations. This viscous region has recently been examined experimentally, and Figure 3 shows the typical  $C_{\text{STATIC}}$  variation in this region as well as the  $C_{\text{STATIC}}$  variation in the inviscid region which was previously discussed. Thus the effect of vorticity shed from the canard of

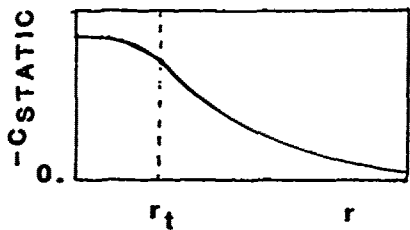


Figure 3. Typical  $C_{\text{STATIC}}$  Behavior with Distance from the Vortex Center

our wind tunnel model induces higher velocities and therefore causes a decrease in local static pressure at points in the flow near that vorticity. Unfortunately, the  $C_{\text{STATIC}}$  coefficient does not allow us to clearly define the edge of the wake. This is evident in Figure 3 where  $r_t$  has been arbitrarily located near the inflection point of the curve.

The  $C_{\text{TOTAL}}$  coefficient, however, can be used to locate the edge of the wake. Bernoulli's equation shows that total pressure is constant in isentropic, incompressible flow. Using our definition,

$$C_{\text{TOTAL}} = \frac{P_{\text{OL}} - P_0}{P_0 - P_\infty},$$

it follows that the coefficient of total pressure in the inviscid region is zero. Since viscosity causes a loss in total mechanical energy,  $P_0$  decreases at radii less than  $r_t$ . As  $P_{\text{OL}}$  drops,  $C_{\text{TOTAL}}$  will decrease to a negative value. Figure 4 approximately shows this behavior. We thus expect the canard wake to appear as a mound with a depression in

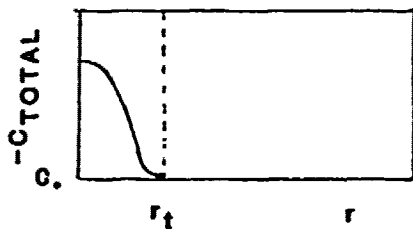


Figure 4.  $C_{\text{TOTAL}}$  (Theoretical) Versus Distance from the Vortex Center

it on the  $C_{\text{TOTAL}}$  contour maps. If we define the edge of the wake as points where the total pressure begins to deviate from free stream, i.e.,  $r_t$ , we have the indicator of the wake location we desire.

An aerodynamic problem associated with the canard wake is the lack of dynamic pressure resulting from viscous losses. If there is a connection between the local dynamic pressure and our definition of  $C_{STATIC}$ , it might also serve to locate the edge of the wake. Our definition is

$$C_{DYN} = C_{TOTAL} - C_{STATIC}$$

Manipulating these equations gives

$$\begin{aligned} C_{DYN} &= C_{TOTAL} - C_{STATIC} = \frac{P_{OL} - P_o}{P_o - P_\infty} - \frac{P_{\omega L} - P_\infty}{P_o - P_\infty} \\ &= \frac{P_{OL} - P_{\omega L} - (P_o - P_\infty)}{P_o - P_\infty} \\ &= \frac{P_{OL} - P_{\omega L}}{P_o - P_\infty} - 1 \end{aligned}$$

$P_{OL} - P_{\omega L}$  is the local dynamic pressure, while  $P_o - P_\infty$  is the free-stream dynamic pressure. Thus,  $C_{DYN}$  is proportional to the ratio of local dynamic pressure to free-stream dynamic pressure.

Since the conditions at infinity approach those of free stream,  $C_{DYN}$  will be approximately zero.  $C_{DYN} = |C_{STATIC}|$  from infinity to  $r_t$  since  $C_{TOTAL} = 0$ . At the center of the vortex, local velocity and thus local dynamic pressure is zero, causing  $C_{DYN}$  to equal -1. From  $r_t$  to the center,  $C_{DYN}$  goes from  $|C_{STATIC}|$  to -1 as in Figure 5. Thus

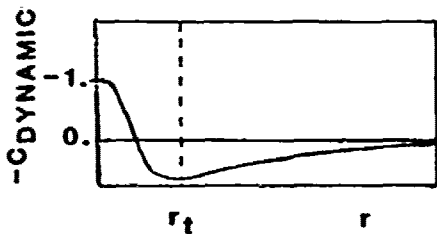


Figure 5.  $C_{DYNAMIC}$  (Theoretical) Versus Distance from the Vortex Center

$C_{DYN}$  also provides an indication of wake location when it reaches the point of its local maximum.

To this point we have considered only a single, isolated two-dimensional vortex. The actual canard wake is much more complex and includes many other factors such as flow separation, multiple vortices, and fuselage interference. We therefore must recognize that this theory only provides us an approximate guide to explain this complex wake behavior.

To measure this complex flow we used a seven-hole probe. Then, using the procedure outlined in Ref. 1, we calculated the angle of attack,  $\alpha$ , sideslip angle,  $\beta$ , and two pressure coefficients  $C_0$  and  $C_\infty$  directly from the seven measured pressures.  $C_{TOTAL}$  and  $C_{STATIC}$  are calculated using  $C_0$  and  $C_\infty$ , and  $C_{DYN}$  is calculated from  $C_{TOTAL}$  and  $C_{STATIC}$ .

After the data is collected and all coefficients are calculated, we graphically display a three-dimensional surface consisting of the Y and Z location of each point and the desired coefficient. The graphs are displayed with either an axonometric or contour projection. (The 1980 Spring/Summer Edition of the Aeronautics Digest displays an axonometric projection on its cover.)

### III. Apparatus

The apparatus we used to perform these tests consisted of a model, seven-hole probe, traverse mechanism, wind tunnel, and data acquisition system.

#### A. Model

The model used in the wind tunnel was a variable-height canard with swept-back wings. The canard was positioned at either a high, middle, or low position. Because of the size of the subsonic wind tunnel used, we utilized a half-span model. This half-span model was a replica of one used at NASA in their Langley Wind Tunnel Facility. The model differs slightly in several linear dimensions from NASA's model because of construction problems. The dimensions of the model with the canard in the low position are shown in Figures 6 and 7.

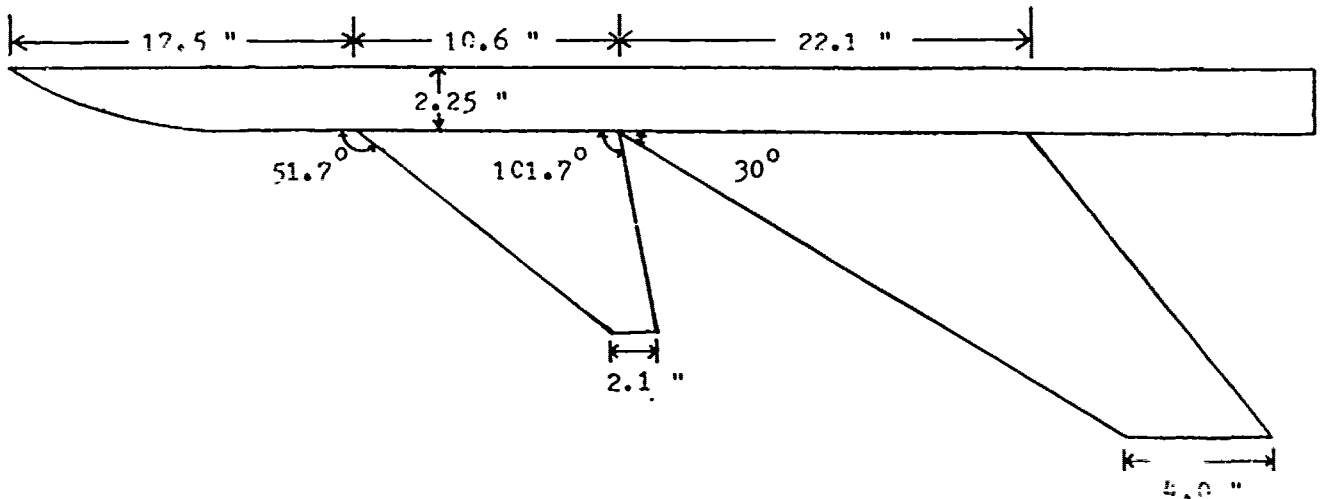


Figure 6. Canard Model (top view)

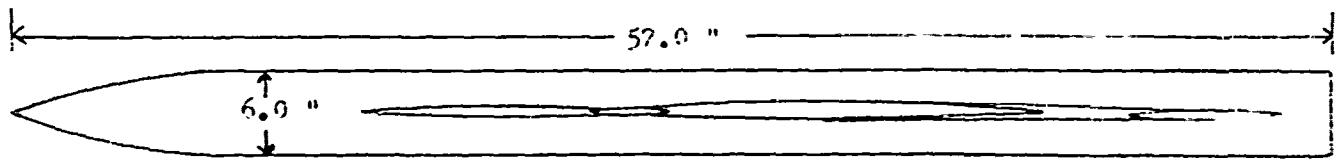


Figure 7. Canard Model (side view)

#### B. Probe

We used the seven-hole probe built by Hollenbaugh and reported by Gallington (Ref. 1). This probe was calibrated last year in the subsonic wind tunnel. The hole arrangement is shown in Figure 8.

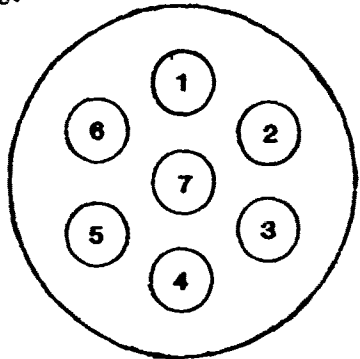


Figure 8. Probe Hole Arrangement

#### C. Traverse Mechanism

We used a previously-designed three-dimensional traverse mechanism and control unit developed by the Frank J. Seiler Research Laboratory for the subsonic wind tunnel. The axes of the traverse are shown in Figure 9. The traverse is computer-driven in the

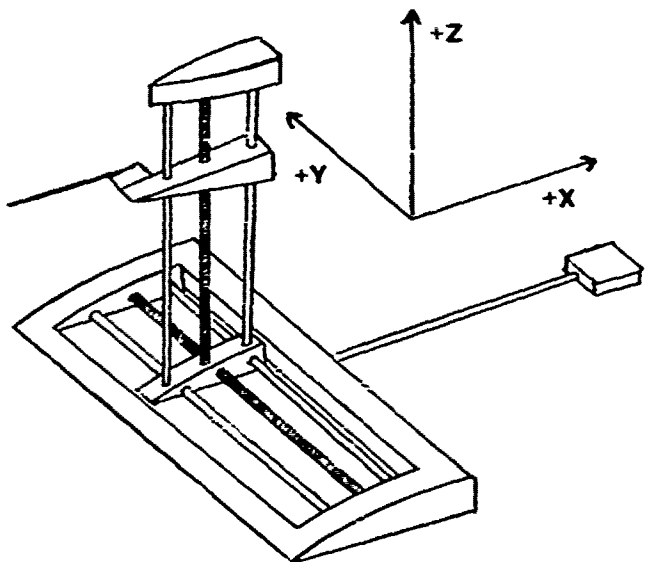


Figure 9. Traverse Mechanism Axes

Y and Z direction and manually controlled in the X direction.

#### D. Wind Tunnel

The experiment used the large closed-circuit wind tunnel which has a two foot by three foot test section and a velocity range from 50 ft/sec to 400 ft/sec at atmospheric pressure. The tunnel is driven by a 200-horsepower synchronous motor coupled with a fluid drive unit which is used to control the RPM of the four-bladed compressor. The tunnel does not have a heat exchanger, which caused tunnel velocity and temperature to increase throughout each run.

#### E. Data Acquisition System

Seven Statham PM6TC ±1-350 transducers were used to convert the probe pressures to voltages. Ten Ectron Model 560 amplifiers were used. A PDP-11/45 computer was used to drive the traverse and collect and reduce the data. The following peripherals and software were used in the data acquisition/reduction process:

- 1) A teletypewriter used as the system list device
- 2) A control/graphic display terminal used to display plots
- 3) A fast access 40-megabyte disk mass storage device
- 4) A system which converts analog signals from the transducers and traverse into digital form suitable for computer use
- 5) Standard graphics software for the display terminal
- 6) A high quality, flat bed pen plotter
- 7) A thermal hard copy device hooked into the display terminal

### IV. Procedure

The actual test procedure can be considered the sequential execution of four computer programs. They were VOLCAL.FTN, TOPWNG.FTN, COEF7.FTN, and SCALAR.FTN. See Appendix A for user instructions for each program. The apparatus had to be installed in the wind tunnel to use the first two programs, but the latter two required only the PDP-11/45 computer.

The first step after the model, traverse, and probe were installed in the wind tunnel was to run VOLCAL.FTN on the computer. VOLCAL used a tri-linear scheme to define the measurement region as a variable number of points on a variable number of planes in a linear prismatic. VOLCAL stored the three-dimensional coordinates of all the points in each plane in a data file, VOLUME.DAT.

The next program, TOPWNG.FTN, drove the probe to each point defined in VOLUME.DAT. It measured the pressures on each of the probe holes along with the tunnel total pressure, static pressure, and temperature. After completely measuring all the points in a given plane, the program wrote the data out to a file called WNGMAP.DAT.

COEF7.FTN reduced all the data stored in WNGMAP.DAT. Seven sets of calibration

coefficients had been previously determined based on the highest of the seven pressures. Two angles and two pressure coefficients were determined from the measured pressures and calibration coefficients which described the local total and static pressures and the local flow angularity (Ref. 1). The reduced data was stored in a file called CONTUR.DAT.

The last program, SCALAR.FTN, produced the graphs. The graphs were projected on the display terminal and hard copies were made on the pen plotter. Both axonometric and contour plots were created.

#### V. Discussion

Data were collected on three different canard wakes using the parametric model described above. Canard positions of 0 inches, 1.125 inches, and 2.75 inches above the plane of the aft-swept wing were investigated. All were at 11 degrees angle of attack. In addition, oil flow visualizations were performed on the high canard model at angles of attack of 11 and 22 degrees. Eight planes of data perpendicular to the free stream were collected for each wake. The oil flows will be discussed first, followed by a discussion of the wakes.

A sketch of the oil flow at 11 degrees angle of attack is shown in Figure 10 and it shows the main features of the flow over the canard and wing. On the canard we see a separation line and a reattachment line. Between the two the oil shows the existence of a large degree of spanwise flow caused by a vortex. This vortex will be called the canard leading edge separation vortex. It exists at the low angle of attack of 11 degrees because the leading edge radius of the canard is near zero. Outside the separation line

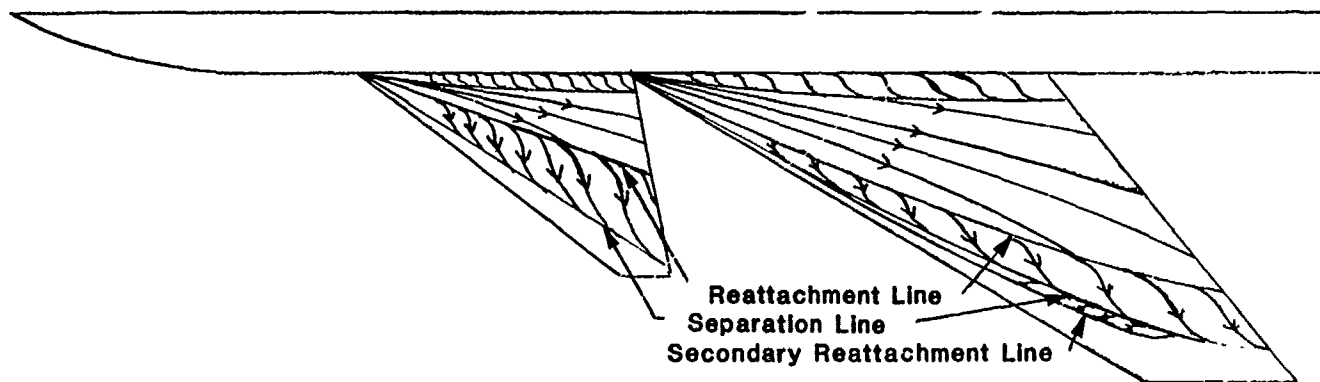


Figure 10. Oil Flow at Alpha = 11 Degrees

the oil has no streaks, indicating the flow is severely separated. To describe this region by potential flow would be very difficult.

On the wing a similar separated flow exists. One different feature is the occurrence of a weak secondary reattachment line outboard of the separation line. The small second-

ary separation vortex which causes this phenomenon is well-documented for highly swept wings (Ref. 4).

The oil flow inside the reattachment line shows the existence of a second, very weak vortex emanating from the non-faired canard-fuselage junction. The oil flow at 22 degrees shows the same results, differing only in the amount of separated flow. Since one of the reasons for mapping these wakes was to aid in their correct potential flow modeling, we chose to concentrate our efforts at 11 degrees angle of attack.

The middle-positioned canard wake will be discussed in detail first. Comparisons with the low- and high-positioned canard wakes will follow.

Contour maps showing lines of constant local total pressure in eight planes of data taken perpendicular to the free stream are presented in Figure 11. The X-axis is parallel to the free stream and therefore is at an 11-degree angle with the longitudinal axis of the fuselage. The Y-axis of the canard is increasing in the inboard direction and its origin is at the trailing edge of the canard tip.

The first plane of data at  $X = .3$  inches behind the canard tip shows a relatively concentrated region of low total pressure inboard and above the canard tip (Figure 11a). The point of minimum pressure marks the center of the canard leading edge separation vortex. Outboard of this is another low-pressure region located above the canard tip, marking the center of the canard tip vortex. These two vortices in such close proximity create a saddle-like structure when plotted in three dimensions (total pressure plotted orthogonally to the Y and Z spacial dimensions). Both vortices are rotating in a clockwise sense when looking into the free stream. The low-pressure regions located seven inches inboard are the result of fuselage-canard interactions because of the lack of well-designed fairing.

As we move aft in Figures 11b through 11h we see the local total pressure and  $C_{TOTAL}$  coefficient increasing as viscous effects reduce the magnitude of velocity gradients in the flow. The integrated total pressure deficit, of course, remains the same.

The relative strengths of the canard tip and separation vortices are evidenced by the magnitudes of the  $C_{TOTAL}$  pressure coefficient and also by the relative movements of the vortex centers. The movement of the canard tip vortex in a clockwise fashion about a point close to the separation vortex center shows the separation vortex is much stronger, inducing more movement in the tip vortex than it can induce in the separation vortex.

In Figures 11e through 11h we see a new structure forming at the bottom and moving outboard as we go aft. This is the wing leading edge separation vortex. The entire structure could not be mapped due to geometric limitations on the traverse mechanism. Figures 11g and 11h show the wing separation vortex is assymmetrical with a small flow structure located inboard. We do not know the cause of this small structure which consistently appears. We suggest that the leading edge separation vortex on a highly swept wing needs to be studied in greater detail.

ary separation vortex which causes this phenomenon is well-documented for highly swept wings (Ref. 4).

The oil flow inside the reattachment line shows the existence of a second, very weak vortex emanating from the non-faired canard-fuselage junction. The oil flow at 22 degrees shows the same results, differing only in the amount of separated flow. Since one of the reasons for mapping these wakes was to aid in their correct potential flow modeling, we chose to concentrate our efforts at 11 degrees angle of attack.

The middle-positioned canard wake will be discussed in detail first. Comparisons with the low- and high-positioned canard wakes will follow.

Contour maps showing lines of constant local total pressure in eight planes of data taken perpendicular to the free stream are presented in Figure 11. The X-axis is parallel to the free stream and therefore is at an 11-degree angle with the longitudinal axis of the fuselage. The Y-axis of the canard is increasing in the inboard direction and its origin is at the trailing edge of the canard tip.

The first plane of data at  $X = .3$  inches behind the canard tip shows a relatively concentrated region of low total pressure inboard and above the canard tip (Figure 11a). The point of minimum pressure marks the center of the canard leading edge separation vortex. Outboard of this is another low-pressure region located above the canard tip, marking the center of the canard tip vortex. These two vortices in such close proximity create a saddle-like structure when plotted in three dimensions (total pressure plotted orthogonally to the Y and Z spacial dimensions). Both vortices are rotating in a clockwise sense when looking into the free stream. The low-pressure regions located seven inches inboard are the result of fuselage-canard interactions because of the lack of well-designed fairing.

As we move aft in Figures 11b through 11h we see the local total pressure and  $C_{TOTAL}$  coefficient increasing as viscous effects reduce the magnitude of velocity gradients in the flow. The integrated total pressure deficit, of course, remains the same.

The relative strengths of the canard tip and separation vortices are evidenced by the magnitudes of the  $C_{TOTAL}$  pressure coefficient and also by the relative movements of the vortex centers. The movement of the canard tip vortex in a clockwise fashion about a point close to the separation vortex center shows the separation vortex is much stronger, inducing more movement in the tip vortex than it can induce in the separation vortex.

In Figures 11e through 11h we see a new structure forming at the bottom and moving outboard as we go aft. This is the wing leading edge separation vortex. The entire structure could not be mapped due to geometric limitations on the traverse mechanism. Figures 11g and 11h show the wing separation vortex is assymmetrical with a small flow structure located inboard. We do not know the cause of this small structure which consistently appears. We suggest that the leading edge separation vortex on a highly swept wing needs to be studied in greater detail.

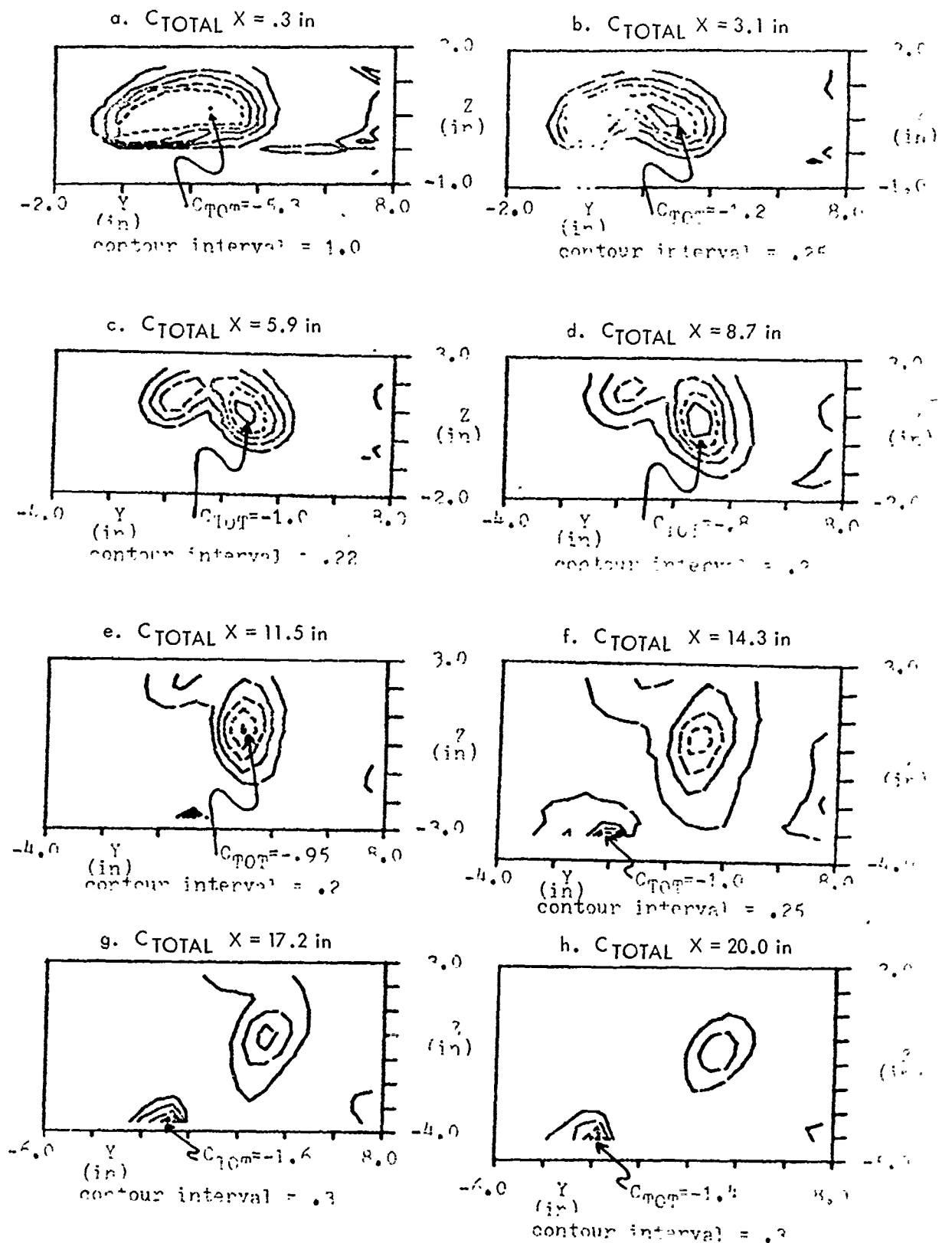


Figure 11. Total Pressure Coefficient

Nowhere in Figures 11a through 11g do we see the effects of the trailing vorticity shed from the canard trailing edge as a result of changes in the spanwise load distribution. It may be that the expected feature has a characteristic dimension that is much smaller than the resolution limit of the probe. This also needs to be studied in more detail.

The approximate locations of the centers of the canard tip and separation vortices versus X are given in Table 1. As we go aft the canard tip vortex goes up and inboard,

Table 1  
CANARD VORTEX CENTER LOCATION

MIDDLE CANARD ALPHA = 11°				
X	TIP		SEPARATION	
	Y	Z	Y	Z
.3	.5	.7	2.7	1.2
3.1	.4	1.0	2.7	1.0
5.9	.2	1.3	2.7	.9
8.7	.2	1.7	2.8	.9
11.5	.3	2.1	2.9	.6
14.3	-	-	3.1	.4
17.2	-	-	3.1	0.0
20.0	-	-	3.1	-.5

while the separation vortex goes down. This downward movement is approximately half the angle of attack.

The local static pressure and static pressure coefficient are inversely related to the magnitude of local velocity. Examining Figure 12a, we see a low-pressure and thus high-velocity flow structure at the Y and Z coordinates (3.5, 1.9). Just below and inboard exists a relatively high-pressure, low-velocity structure forming a "static pressure doublet." One possible explanation for this structure is that the low-velocity region represents the vortex core with its region of rigid body rotation. If the high velocity represents the edge of the viscous-potential flow boundary, by theory it should encircle the vortex core. The fact that it does not suggests the answer may be that the characteristic of the flow structure is less than the resolution limit of the probe. This may also be causing the discrepancy between the center of the low-velocity region and the center of the total pressure loss. The resolution limit needs to be quantified.

An interesting feature of the static pressure map is the linear, high-pressure/low-velocity ridge located between points (0, .3) and (3.5, .3). This appears to be the wake of the shed vorticity from the canard trailing edge because of changes in the spanwise load distribution. If we examine static pressures on a line perpendicular to this structure we see a low-pressure/high-velocity region, a high-pressure/low-velocity wake, and a low-pressure/high-velocity region below. This classic wake structure is quickly dissipated as we go aft because of viscous effects.

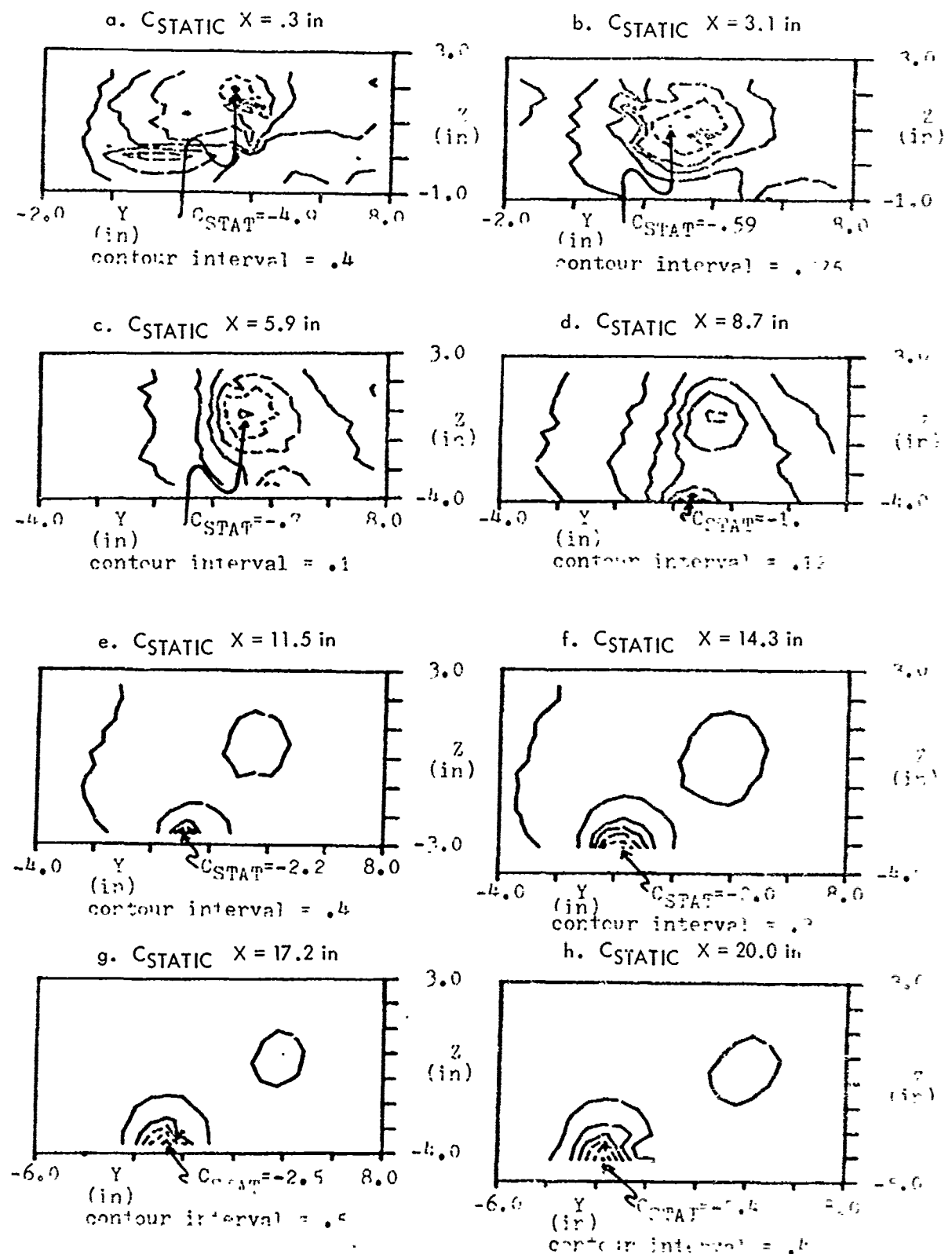


Figure 12. Static Pressure Coefficient

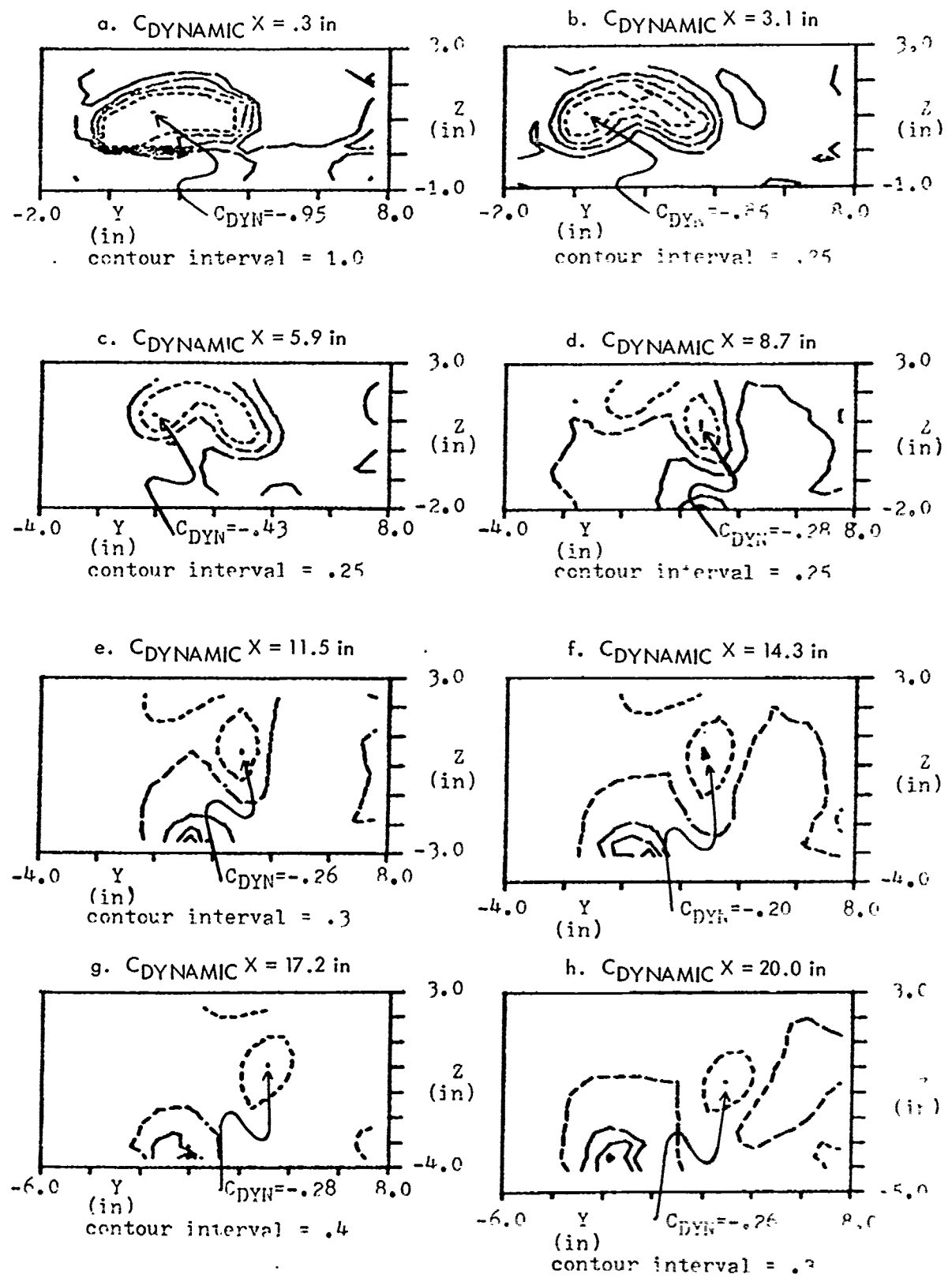


Figure 13. Dynamic Pressure Coefficient

Examining the rest of Figure 12, we see that the major features of the flow are the canard leading edge separation vortex in the center and the wing separation vortex below it. A third feature that deserves comment is the shape of the static pressure contours outboard of the vortices, which is essentially a series of parallel lines. This means the flow velocity inboard is higher than outboard in a regular fashion. This is due to the induced flow field of the 60-degree swept wing. The inboard portion of each figure is above the wing surface while the outboard portion is in front of the leading edge. We expect the velocity above the wing to be higher than the induced velocity in front of the leading edge.

The local dynamic pressure is presented in Figure 13 as contour plots of the dynamic pressure coefficient. Since this coefficient is simply the difference of the total and static pressure coefficients, it shows the features of both. Figure 13a illustrates the effect of the linear canard wake ridge observed in Figure 12a. The high and low "static pressure doublet" causes only very slight modification to the upper right side of the total pressure structure of Figure 11a. Figures 13b through 13h behave as expected.

Two other canard wakes were mapped with the canard at 0 inches and 2.75 inches above the plane of the wing. Since these wakes gave very similar results to the middle canard, we will summarize the total pressure data by giving the coordinates of the canard leading edge separation vortex and tip vortex in Tables 2 and 3. The origin of the coordinate system for all three tables is the same.

Table 2  
CANARD VORTEX CENTER LOCATION

LOW CANARD ALPHA = 11°				
X	TIP		SEPARATION	
	Y	Z	Y	Z
.3	.4	-.3	2.1	0.0
3.1	.2	-.1	2.1	.3
5.9	0.0	.4	2.2	-.3
8.7	.1	.8	2.5	0.0
11.5	.	1.4	2.7	-.2
14.3	-	-	3.0	-.5
17.2	-1.8	1.8	3.0	-1.0
20.0	-	-	3.0	-1.3

Table 3  
CANARD VORTEX CENTER LOCATION

HIGH CANARD ALPHA = 11°				
X	TIP		SEPARATION	
	Y	Z	Y	Z
.2	-1.0	2.3	2.1	2.6
3.1	- .4	2.6	2.5	2.4
5.9	0.0	2.8	2.8	2.1
8.8	-	-	3.0	1.8
11.7	-	-	3.0	1.6
14.6	-	-	3.0	1.6
17.4	-	-	3.0	1.3
20.3	-	-	3.2	1.0

#### VI. Conclusions

We have documented the development and use of a new technique of conducting flow field surveys using a seven-hole probe. These surveys allow the calculation of most of the important flow field parameters, including local static and total pressures. This technique was used to survey the canard wake of three separate models at subsonic incompressible speeds. Our results allow us to locate the canard wakes passing above the wing surface. They also indicate a possible discrepancy of location of wakes depending on the type of data examined, that is, static, total, or dynamic pressure. The relative accuracy of the method is undetermined as is the resolution limit of the probe and the frequency response of the apparatus. The tests were run only at incompressible flow velocities. Despite these criticisms, a valuable educational and research technique for quantitative flow field visualization has been developed.

#### References

1. Gallington, R. W. "Measurement of Very Large Flow Angles With Non-Nulling Seven-Hole Probes." Aeronautics Digest - Spring/Summer 1980, USAFA-TR-80-17, USAF Academy, Colorado.
2. Clancy, L. J. Aerodynamics. New York: John Wiley & Sons, 1975.
3. Panton, R. L., W. L. Oberkampf, and N. Soskic. "Flight Measurements of a Wing Tip Vortex." Journal of Aircraft, Vol. 17, No. 4 (1980), Article No. 80-4030.
4. Kulfan, R. M. "Wing Airfoil Effects on the Development of Leading-Edge Vortices." AIAA Paper, 79-1675.

## Appendix A

This appendix contains the user instructions for VOLCAL.FTN, TOPWNG.FTN, COEF7.FTN, and SCALAR.FTN. All the left-justified capitalized lines are either responses to or replies from the PDP-11/45 computer.

### VOLCAL.FTN USER'S MANUAL

ENTER A HEADING FOR THE GRAPHS GENERATED BY SCALAR.FTN. DESCRIBE THE MODEL CONFIGURATION, THE ANGLE OF ATTACK, AND ANY OTHER DESIRED INFORMATION. MAX LENGTH IS 40 CHARACTERS.

The user now enters a heading such as

ALPHA = 11 MIDDLE CANARD, SWEPT BACK WING

The computer then prints out what is entered and asks if it is correct. If correct, Y is entered. If incorrect, N is entered and the computer again requests the title information.

ENTER XA, YA, ZA

The computer asks for the X, Y, and Z coordinates for corner point A. Figure A-1 shows the location of points A through H. The dimensions of each coordinate are

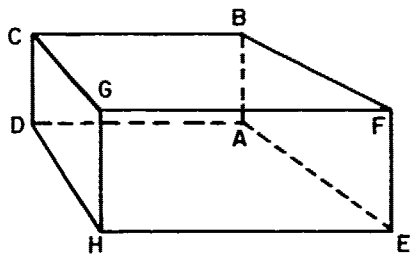


Figure A-1. Measurement Volume

in inches and are referenced to the (0,0,0) point at the outboard tip of the middle canard. Point A is the lower right corner of the volume as referenced to the front of the model.

ENTER XB, YB, ZB

.....

ENTER XH, YH, ZH

ARE THESE CORRECT? (Y OR N)

If N is entered, the computer asks for the coordinates again.

ENTER THE DESIRED NUMBER OF PLANES OF DATA IN THE X DIRECTION, THE NUMBER OF POINTS DESIRED IN THE Y DIRECTION (OUT THE CANARD TIP), AND THE DESIRED NUMBER OF POINTS IN THE Z DIRECTION, RESPECTIVELY. USE REAL FORMAT.

We used four planes of data in the X direction, 20 points in the Y direction, and 14 points in the Z direction. The input was thus:

4,20,14

The computer then prints out the values entered above and asks if they are correct. If N is entered, then it will go back and ask the above question again. The program now executes to completion.

#### TOPNG.FTN USER'S MANUAL

##### ENTER VOLUME.DAT VERSION NUMBER

The user now enters the version number of VOLUME.DAT that corresponds to the model configuration being tested.

##### ENTER TEMP, PADM (USE REAL FORMAT)

The user enters the room temperature ( $^{\circ}$ F) and the room pressure (in. Hg). After the temperature and pressure are entered, the computer prints them out and asks if they are correct.

##### START TUNNEL AND ENTER GO WHEN READY

The user starts the tunnel and enters GO when the air is stabilized at the desired velocity.

##### ENTER WHAT VELOCITY THE RUN IS AT AND ANY OTHER INFORMATION UP TO A TOTAL OF 20 CHARACTERS LONG YOU WISH TO HAVE IN THE GRAPH TITLE

The user enters something similar to

##### VEL = +100 FPS

The computer prints out the above and checks if it is correct. If incorrect, the user enters N and the computer asks for it again.

THE NEXT PLANE THAT IS RUN IS AT X = .3. DO YOU WANT TO RUN THIS PLANE OF DATA? IF YOU DO, MOVE THE PROBE TO THE DISPLAYED X VALUE AND ENTER GO. IF YOU WANT ANOTHER PLANE, THEN ENTER NO.

The user acts accordingly. As soon as GO is entered, the program will start taking data. When a plane is completed, the following message is printed out on the screen if there is another plane of data to be taken.

MOVE TRAVERSE MECHANISM TO NEXT X VALUE, X = 3.1.

ENTER GO WHEN READY TO CONTINUE RUN.

As soon as GO is entered, the program takes another plane of data. The computer carriage returns when it completes the last plane of data.

#### COEF7.FTN USER'S MANUAL

##### ENTER WNCMAP.DAT VERSION NUMBER

The user enters the version number of the WNCMAP.DAT data file to be reduced.

#### SCALAR.FTN USER'S MANUAL

##### DO YOU WANT AN HP-4662 HARDCOPY?

If the user wants a hard copy, he sets up the 4662 printer with the paper, defines the borders (if needed), and enters Y. N is entered if the user wants the graph

displayed on the screen.

ENTER CONTUR.DAT VERSION NUMBER

The user enters the corresponding version number of the plane of data to be displayed.

ENTER VALUE FOR Z COORDINATE DATA

1 CA

2 CB

.

.

.

13 CDYN

The user enters the number of the data to be displayed.

ENTER A1,A2,A3,S1,S2,S3

The user enters 0, 120, 90, .4, .4, .4, 1 if an axonometric projection is desired or 0, 90, 0, .4, .4, .4 if a contour projection is desired. The three .4's are the scaling factors. Changing these will change the size of the graph.

If a contour projection is selected, the computer will print out:

ZMIN	ZMAX	INC
-1.235	.243	.215

DO YOU WISH TO CHANGE LIMITS?

If more or less intervals are desired, the user enters Y. If the given intervals are satisfactory, N is entered. If Y is entered, the computer will print out:

ENTER ZLOW, ZMAX, ZINC

The user now enters the required information such as

-1.2, .2, .3

The program now plots the graph either on the terminal screen or on the 4662 flat bed pen plotter.